Effect of 3D magnetic perturbations on divertor conditions and detachment in tokamak and stellarator

You may also be interested in:

Monte-Carlo fluid approaches to detached plasmas in non-axisymmetric divertor configurations
Y Feng, H Frerichs, M Kobayashi et al.

Characterization of divertor footprints and the pedestal plasmas in the presence of applied n=3 fields for the attached and detached conditions in NSTX
J-W Ahn, F Scotti, K Kim et al.

Changes in divertor conditions in response to changing core density with RMPs
A.R. Briesemeister, J.-W. Ahn, J.M. Canik et al.

Control of 3D edge radiation structure with resonant magnetic perturbation fields applied to the stochastic layer and stabilization of radiative divertor plasma in LHD
M. Kobayashi, S. Masuzaki, I. Yamada et al.

Divertor program in stellarators
R König, P Grigull, K McCormick et al.

Resonant magnetic perturbations of edge-plasmas in toroidal confinement devices
T E Evans

Understanding edge-localized mode mitigation by resonant magnetic perturbations on MAST
A. Kirk, I.T. Chapman, Yueqiang Liu et al.

Effect of resonant magnetic perturbations on ELMs in connected double null plasmas in MAST
A Kirk, Yueqiang Liu, I T Chapman et al.

Effect of 3D magnetic perturbations on divertor conditions and detachment in tokamak and stellarator

J-W Ahn[1], A R Briesemester[1] , M Kobayashi[2], J D Lore[1], O Schmitz[3],
A Diallo[4], T K Gray[1], C J Lasnier[5], B P LeBlanc[4], R Maingi[4], A G McLean[5],
S A Sabbagh[6] and V A Soukhanovskii[5]

[1] Oak Ridge National Laboratory, Oak Ridge, TN 37831, United States of America
[2] National Institute for Fusion Science, Toki 509-5292, Japan
[3] University of Wisconsin—Madison, Madison, WI 53706, United States of America
[4] Princeton Plasma Physics Laboratory, Princeton, NJ 08540, United States of America
[5] Lawrence Livermore National Laboratory, Livermore, CA 94550, United States of America
[6] Columbia University, New York, NY 10027, United States of America

E-mail: jahn@pppl.gov

Abstract

Enhanced perpendicular heat and momentum transport induces parallel pressure loss leading to divertor detachment, which can be produced by the increase of density in 2D tokamaks. However, in the 3D configurations such as tokamaks with 3D fields and stellarators, the fraction of perpendicular transport can be higher even in a lower density regime, which could lead to the early transition to detachment without passing through the high-recycling regime. 3D fields applied to the limiter tokamak plasmas produce edge stochastic layers close to the last closed flux surface (LCFS), which can allow for enhanced perpendicular transport and indeed the absence of high recycling regime and early detachment have been observed in TEXTOR and Tore Supra. However, in the X-point divertor tokamaks with the applied 3D fields, the parallel transport is still dominant and the detachment facilitation has not been observed yet. Rather, 3D fields affected detachment adversely under certain conditions, either by preventing detachment onset as seen in DIII-D or by re-attaching the existing detached plasma as shown in NSTX. The possible way for strong 3D effects to induce access to the early detachment in divertor tokamaks appears to be via significant perpendicular loss of parallel momentum by frictional force for the counter-streaming flows between neighboring flow channels in the divertor. In principle, the adjacent lobes in the 3D divertor tokamak may generate the counter-streaming flow channels. However, an EMC3-EIRENE simulation for ITER H-mode plasmas demonstrated that screened RMP leads to significantly reduced counter-flows near the divertor target, therefore the momentum loss effect leading to detachment facilitation is expected to be small. This is consistent with the observation in LHD, which showed screening (amplification) of RMP fields in the attachment (stable detachment) case. Work for optimal parameter window for best divertor operation scenario is needed particularly for the 3D divertor tokamak configuration.

Keywords: detachment, 3D fields, RMP, plasma response, diverter plasma regime, 3D effects on divertor

(Some figures may appear in colour only in the online journal)

1. Introduction

Externally applied non-axisymmetric, i.e. 3D, magnetic perturbations have been widely used for various physics purposes in tokamaks such as edge localized mode (ELM) suppression/mitigation [1–7], neoclassical toroidal viscosity control [8, 9], and the generation of non-resonant magnetic field assisted QH-mode plasmas [10, 11], etc. While the control of transient heat flux from ELMs are critical for the success of ITER and beyond, steady state heat flux control is also an important requirement for the operation of long-pulse, high performance H-mode plasmas, in order to keep the peak heat flux (q_{peak}) under $\sim 10\,\mathrm{MW\,m^{-2}}$. Mitigation of steady state heat flux via divertor detachment is a leading candidate to achieve this goal. Divertor detachment is a physical process of increased radiation power along with rapid cooling of divertor plasma that leads to pressure drop along the flux tube, caused by increased density of main ions or impurity seeding. The interaction of applied 3D fields with divertor plasma and detachment has been intensively investigated in recent years in tokamak [12–24] and stellarator [25–30]. The ultimate goal is the simultaneous achievement of divertor detachment and ELM suppression but this has not been accomplished in any machine yet.

The applied 3D fields interact with the plasma to be shielded or amplified by plasma response, with the response behavior affected by several parameters such as toroidal mode number (n) of the 3D fields, q_{95}, and the normalized beta (β_{N}), etc. The plasma response to the 3D fields determines how the applied 3D fields penetrate through the plasma surface and generate magnetic islands or a layer of stochastic magnetic fields. The magnetic separatrix is also perturbed by 3D fields and is split into multiple invariant manifolds to form a 3D lobe structure for open field lines [31, 32]. Stochastic field lines from the plasma boundary tangle into the lobes and carry hot and dense plasma particles from inside the separatrix, which induces non-axisymmetric heat and particle flux, represented as a striated deposition pattern, at the divertor surface. These lobes can shrink or be amplified by plasma response and the observed striation pattern can be very different from the vacuum approximation result. The role of plasma response inside the separatrix, calculated with the ideal response model such as IPEC [33] or resistive response model such as M3D-C1 [34], was demonstrated in the field line tracing by comparing different toroidal mode numbers and coil configurations, which significantly altered the footprint pattern. For example, in NSTX, plasma response shielded $n = 3$ perturbations but the envelope of striations was largely unchanged compared to the vacuum modeling [12–14, 35]. However, $n = 1$ response dramatically amplified 3D footprints [35]. In DIII-D, the even parity configuration for $n = 3$ primarily shielded applied 3D fields but the odd parity amplified them, relative to the results from vacuum modeling, leading to shrinking and amplification of experimentally observed lobes compared to vacuum 3D footprints respectively [15, 17, 36]. The measured plasma response in large helical device (LHD) shows that applied resonant

magnetic fields (RMPs) are shielded in the attached divertor phase and amplified in the detached phase [25, 37, 38].

Since the tokamak plasma is no longer axisymmetric with the applied 3D fields, common elements with stellarator physics have been also explored recently. Note that the 3D structure of boundary plasma for the limiter tokamak (i.e. LCFS is defined by the contact of plasma with material surface when there is no 3D perturbation) is very different from that of the divertor tokamak (LCFS is defined by the magnetic separatrix formed by X-point). For the limiter geometry, the applied 3D fields produce stochastic and laminar regions near the LCFS and the primary channel of transport to the wall is the radial component of perpendicular and parallel transport with respect to stochastic field lines. For the divertor geometry, however, 3D fields induce island overlap that generates a stochastic layer and the magnetic separatrix is split into several 'lobes', each of which intersects with the divertor surface. Unlike the limiter geometry, this magnetic configuration produces a situation that parallel flux and the poloidal component of perpendicular flux are the primary channel for the transport between LCFS and the divertor plates. These differences lead to different behavior of boundary plasma in response to 3D fields, therefore the effect on detachment is also differentiated. In this review, we define 3D effects on the boundary plasma to emerge when the perpendicular transport (for heat, particle, and momentum) becomes comparable to the parallel transport.

Given the importance of controlling both the transient and steady state divertor heat and particle flux in ITER in the presence of 3D fields, it is crucial to understand the status and to identify outstanding issues on the effect of 3D fields on the divertor conditions and detachment. In particular, how the 3D fields affect physical processes leading to the change in divertor conditions and detachment, what are the key parameters for the effects, and then how to control and optimize divertor heat flux behavior by 3D fields, are the three important issues that should be addressed. Consistent explanation for these questions is necessary for tokamak machines first, and similarities and differences between the 3D tokamak and stellarator should be studied to identify the underlying physics issues.

Various aspects of 3D effects on the divertor plasma in tokamaks and stellarators, with focus on heat flux footprints and detachment, will be reviewed and discussed in this paper. Conventional detachment induced by gas puff will be only considered here and those from magnetic configuration change, such as snowflake divertor [39, 40], are out of scope of this review. Data from two tokamak machines (NSTX and DIII-D) and one stellarator (LHD) will be primarily shown and discussed. Section 2 will describe experimental observation of 3D effects on divertor footprint behavior, along with related core plasma parameters, as a function of density up to the detachment onset and beyond. All data are from H-mode plasmas in the X-point divertor configuration in NSTX and DIII-D. These results are also compared to 3D transport simulations to deduce physical interpretations. Results from LHD helical divertors for both experiment and modeling, including the role of plasma response, are presented in
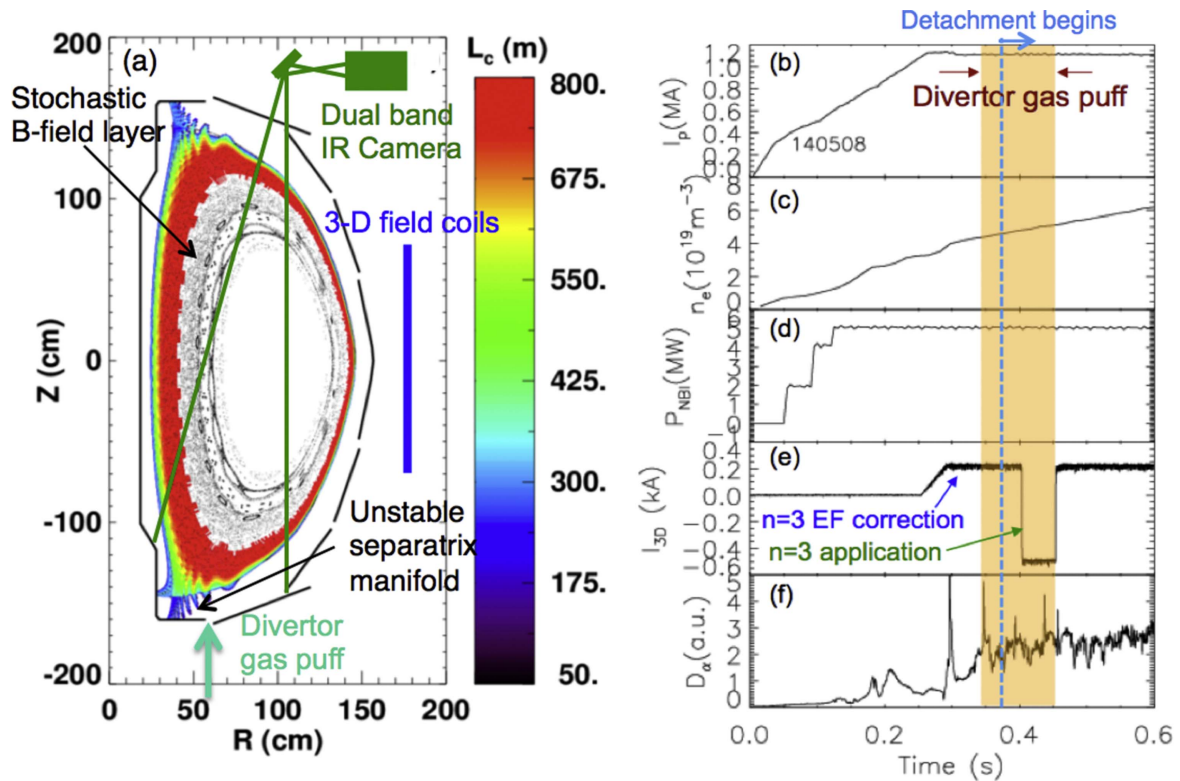
Figure 1. (a) Poloidal cross section of connection length of field lines in NSTX, calculated with vacuum approximation for $n = 3$ perturbation, with IR camera, 3D field coils, and divertor gas puff location overlaid. Time trace of several operational parameters taken during a divertor detachment and 3D field application experiment in NSTX (in the same series of discharges shown in figures 2–4); (b) plasma current, (c) line average density, (d) NBI power, (e) 3D field coil current, and (f) D_α signal at lower divertor. The $n = 3$ perturbation fields are superimposed onto the $n = 3$ error correction fields for the 2nd half ($t = 0.4$–0.45 s) of the detachment period ($t = 0.35$–0.45 s, orange shadow). Figure 1(a) is based on the figure 3(a) in [22]. Plots (b)–(f) were reproduced with permission from [14]. © IOP Publishing Ltd. All rights reserved.

section 3. Section 4 is dedicated to more general aspect of 3D effects on divertor transport and detachment, where a brief description of the prospect for ITER is also presented. Finally, summary and discussion is given in section 5.

2. Effect of 3D fields on detachment for X-point divertor tokamak

2.1. Effect of applied 3D fields on divertor and pedestal plasmas in NSTX

2.1.1. Setup and diagnostics. NSTX has a total of six ex-vessel 3D field coils at the mid-plane, see figure 1(a), which enables the application of $n = 1, 2, 3$ magnetic perturbations. For 3D detachment experiments, $n = 3$ configuration was used and a poloidal cross section of Poincare plot using the vacuum field line tracing for $n = 3$ case is overlaid in figure 1(a), where the stochastic magnetic field layer in the boundary region and unstable separatrix manifolds are visible. Typical time traces of main plasma parameters during the experiment are shown in figures 1(b)–(f). Deuterium gas is injected through the gap in the lower divertor area for a period of 100 ms to induce detachment. $n = 3$ fields are applied for the 2nd half of the divertor gas puff period, on top of ~ 0.2 kA of $n = 3$ error field correction fields, figure 1(e). In RMP

experiments in other tokamaks, a decrease of line average electron density by applied 3D fields (the 'density pump-out') is often observed, which is attributed to the decrease of pedestal density [41, 42] by 3D fields, but this is generally not observed in NSTX as seen in figure 1(c).

The divertor plasma is monitored by several diagnostics for detachment and 3D effects, including a 2D dual band infrared (IR) camera [43, 44] for heat flux footprints, two wide-angle visible cameras [45] for D_α and Li–I intensity as a proxy to particle flux footprints, a 1D ultraviolet-visible-near infrared divertor imaging spectrometer [46] for high-n Balmer line emission (indicative of divertor volume recombination, typical for radiative/detached divertor condition).

2.1.2. Effect on divertor and pedestal plasma. The amount of deuterium gas for divertor injection was varied, from 2000 Torr of gas pressure ($\sim 7 \times 10^{21}$ D sec^{-1} of particle flow rate) to 4000 Torr ($\sim 16 \times 10^{21}$ D sec^{-1} of flow rate) to create different level of divertor detachment. After the gas puff begins at $t = 350$ ms (see the time traces in figure 1), the transition from the attached to the detached divertor plasma occurs at $t = 370$–380 ms for all gas level cases. Both the electron temperature (T_e) and density (n_e), and the ion temperature (T_i) in the pedestal region decrease as the detachment progresses, and the reduction becomes larger with
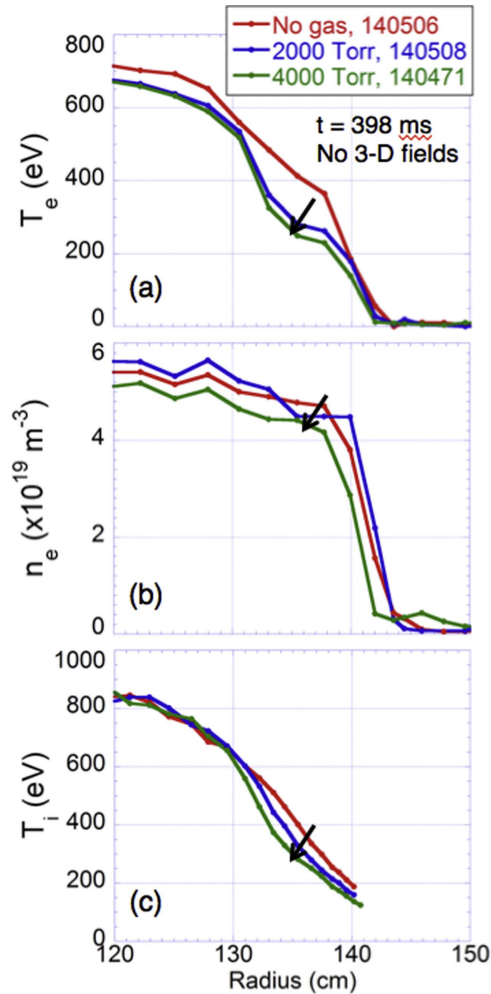
Figure 2. Profile of electron temperature (a), density (b), and ion temperature (c) for no gas puff (red), 2000 Torr of divertor gas puff (blue), and 4000 Torr of gas puff (green). It is seen that all pedestal profiles decrease progressively with the increase of gas puff.

higher gas puff (see figure 2). This is also reflected in the evolution of the total stored energy (W_{tot}), i.e. the W_{tot} drop is larger for the higher gas puff cases (see figure 4(d)). Figure 3 shows 2D heat flux profiles mapped to the (r, ϕ) coordinate before gas puffing (plots in 1st column, attached condition), after gas puffing (2nd column, detached), and after 3D field application during gas puffing (3rd). All heat flux profiles before gas puff (figures 3(a), (d) and (g)) show a peak near the strike point ($r \sim 0.4$ m), which is typical for attached divertor. After puffing gas into divertor, heat flux near the strike point is reduced by $\sim 80\%$ (<1 MW m^{-2}) while heat flux farther from the strike point ($r \gtrsim 0.45$ m) still remains at ~ 2 MW m^{-2}. This is the partial detachment where plasma near the strike point detaches first before it fully detaches over the whole divertor area. However, for the highest gas pressure of 4000 Torr, it is seen that heat flux in the far scrape-off layer (SOL) region is also reduced significantly (see figure 3(h)), indicating that the divertor plasma is fully detached.

Figures 3(c), (f) and (i) are after $n = 3$ fields were applied during detachment. The striking observation for low gas pressure (2000 Torr) is that heat flux striations burn

through detachment and re-attach the divertor plasma, see figure 3(c). This leads the heat flux profile to peak again near the strike point with local peaks and valleys in the SOL region, although the heat flux value at the strike point, i.e. q_{peak}, is lower than that before the gas puffing, i.e. ~ 3.5 versus ~ 5 MW m^{-2}. When the gas pressure was raised to 3000 Torr, partial detachment is still maintained even after the 3D field application (figure 3(f)), i.e. heat flux near the strike point is kept reduced (<1 MW m^{-2}). However, 3D fields cause heat flux striations in the far SOL region (indicated by the yellow circle), noticeably higher than the level without 3D fields seen in 2(e). This shows that magnetic lobes still impose substantial non-axisymmetric heat flux, some of which goes to the outer region of divertor surface even during the near SOL detachment. These striations are eventually eliminated when the highest pressure of gas injection (4000 Torr) was used; figure 3(i) illustrates that 3D fields now have no impact on divertor detachment. Note that high-n Balmer line emission intensity also shows [14] the same behavior demonstrated in figure 3. Data in figure 3 show that the applied 3D fields become less effective with the increase of gas puff.

Moving to the pedestal plasma, various plasma parameters have been investigated and a previous study shows that [14] the pedestal T_e ($T_{e,ped}$) is the most relevant parameter affecting the behavior of 3D footprints for the cases shown in figure 3. Figure 4 shows the change of $T_{e,ped}$ across the gas puff and 3D field application period for three different gas levels. As the detachment of divertor plasma is established by gas puff, $T_{e,ped}$ drops progressively with the gas puff. In the case of re-attachment by 3D fields for the 2000 Torr gas puff as shown in figure 3(c), $T_{e,ped}$ rises back up after the application of 3D fields (see figure 4(a)), while $n_{e,ped}$ remains unaffected [14]. The restoration of $T_{e,ped}$ is consistent with the drop of pedestal electron heat diffusivity ($\chi_{e,ped}$) shown by a TRANSP calculation [14]. For higher gas puff cases where no re-attachment was observed, $T_{e,ped}$ remained reduced before and after turning on the 3D field, so the applied 3D field had no effect on $T_{e,ped}$, see figures 4(b) and 3(c). Figure 4(d) is the temporal evolution of total stored energy (W_{tot}) for the cases discussed above. It is seen that divertor gas puff reduces W_{tot} with the onset of detachment and higher gas puff induces larger decrease of W_{tot}. However, W_{tot} was restored from $t \sim 425$ ms (red trace in figure 4(d)) after applying 3D fields for the 2000 Torr case (note that the reduction of W_{tot} for $t \sim 437$–447 ms appears to have been caused by a large ELM that occurred at $t \sim 436$ ms). This is consistent with the $T_{e,ped}$ restoration and divertor re-attachment by 3D fields, shown in figures 4(a) and 3(c) respectively. Given that n_e or T_i restoration was not observed even in the 2000 Torr case [14], the increase of W_{tot} by 3D fields is attributed to the increase of $T_{e,ped}$. For higher gas puff cases (i.e., 3000 and 4000 Torr), the W_{tot} restoration by 3D fields was not observed; see blue and green trace in figure 4(d). It is thought that the apparent beginning of W_{tot} increase at $t \sim 400$ ms for the 4000 Torr case (green trace) is not due to the 3D fields but is just a consequence of natural plasma evolution, as a similar W_{tot}
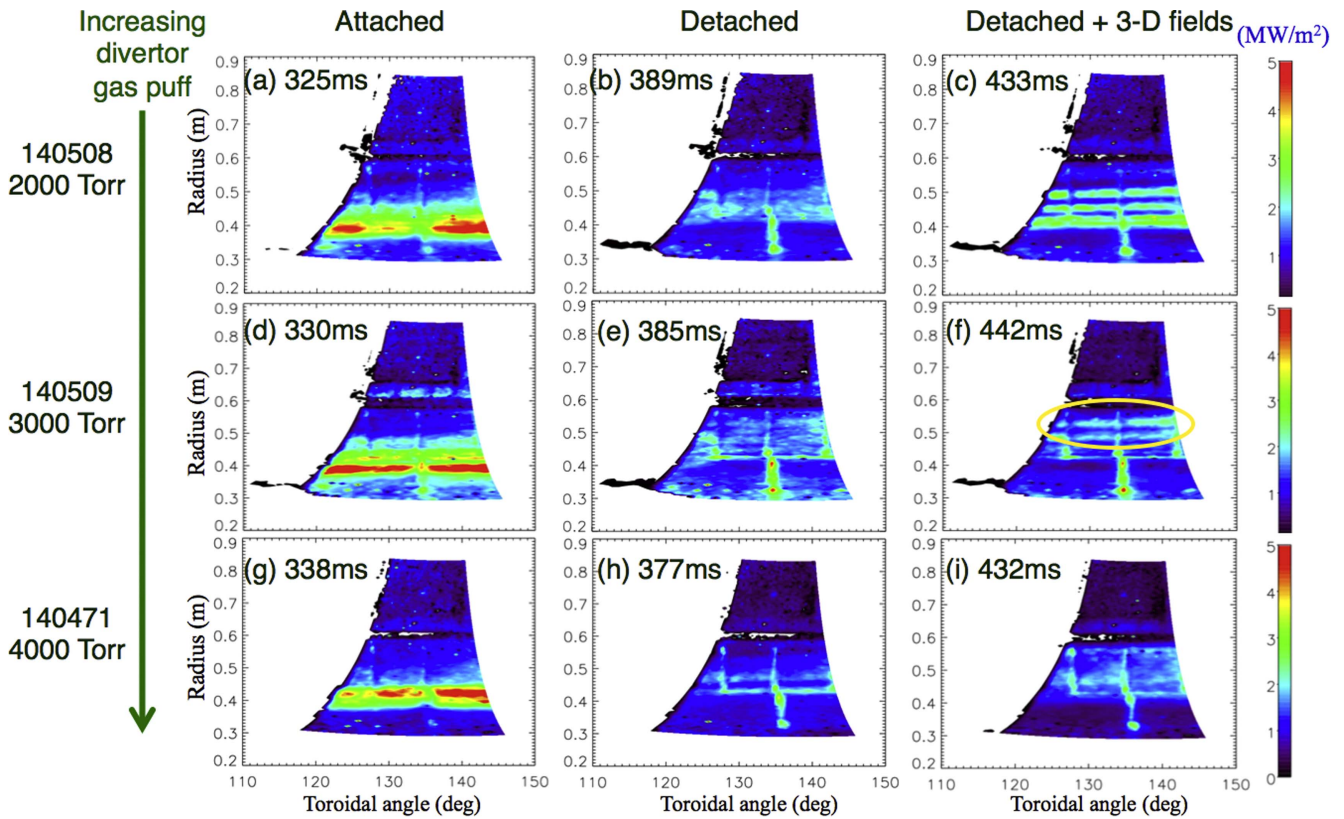
Figure 3. 2D heat flux profile for 3 levels of divertor gas puff in NSTX. Plots (a)–(c) are for low gas puff (2000 Torr), (d)–(f) are for the medium (3000 Torr), and (g)–(i) are for the high gas puff (4000 Torr) case. Divertor gas puff was for $t = 350$–450 ms for all three cases. Plots in the left column represent the attached divertor condition before gas puff, while those in the middle column show a partially detached condition, i.e. detached particularly near the strike point ($r \sim 0.4$ m). Plots in the right column show the effect of applied 3D fields on the detachment.

increase begins at $t \sim 390$ ms (before the 3D fields) for the 3000 Torr case (blue trace).

2.1.3. EMC3-EIRENE simulation. The EMC3-EIRENE code [47, 48] is a coupled 3D Monte Carlo plasma fluid transport (EMC3) and kinetic neutral recycling and transport (EIRENE) package. The code includes transport of particles, electron and ion energy, and parallel momentum in stochastic fields with 3D plasma-facing component geometries. It was first applied to stellarators [47, 48] and later extended to poloidally diverted tokamaks including NSTX [22–24] and DIII-D [49–51]. An $n = 3$ configuration was used for the simulation of NSTX with the use of the B-field in the vacuum approximation, where the perturbed field consists of a wide region of destroyed flux surfaces and helical lobes as seen in figure 1(a). The intersection of the lobes with the divertor results in a striated flux footprint pattern on the target plates. Profiles of divertor heat and particle fluxes were compared with experimental data, with reasonable reproduction of the trend found in the measurement [22].

A series of EMC3-EIRENE simulations with density scan in NSTX was made to validate against experimental trend described in section 2.1.2, again using vacuum approximation [23, 24]. Figure 5 shows the results using the equilibrium file for the 2000 Torr case in figures 3 and 4, and compares ion particle flux (Γ) onto the divertor target,

total power to the target (P_{targ}), and average T_e at the target between with and without 3D fields ($n = 3$). Above $n_e = 5 \times 10^{19}$ m^{-3}, target particle flux rapidly drops, a typical signature of divertor detachment, without 3D fields. However, this particle flux roll-over is not observed in the presence of $n = 3$ fields and it continues to increase with density over the range tested, which indicates that the divertor plasma remains in the high-recycling regime (figure 5(a)). This demonstrates an increase in the density required to achieve detachment, consistent with the experimental divertor re-attachment by 3D fields for low gas puff case, as shown in figures 3(c) and 4(a). Also, divertor power and target T_e do not continue to decrease past $n_e = (4$–$5) \times 10^{19}$ m^{-3} when $n = 3$ fields are applied, see figures 5(b) and (c). Figure 6 shows comparison of divertor heat flux profile for three density levels with and without 3D fields ($n = 3$). As the density is increased, the axisymmetric case shows decrease of peak heat flux and eventually transitioning to detachment at highest density. However, in case of 3D fields, local peaks in heat flux profile at larger major radius remain even as the primary peak is reduced with the increase of density, same as the experimental trend shown in figures 3(d)–(f).

This trend seen both in the experiment and simulation raises a concern about the level of steady state heat flux in the presence of 3D fields if extrapolated to ITER. The striations on the outer side of the divertor surface, while the near SOL
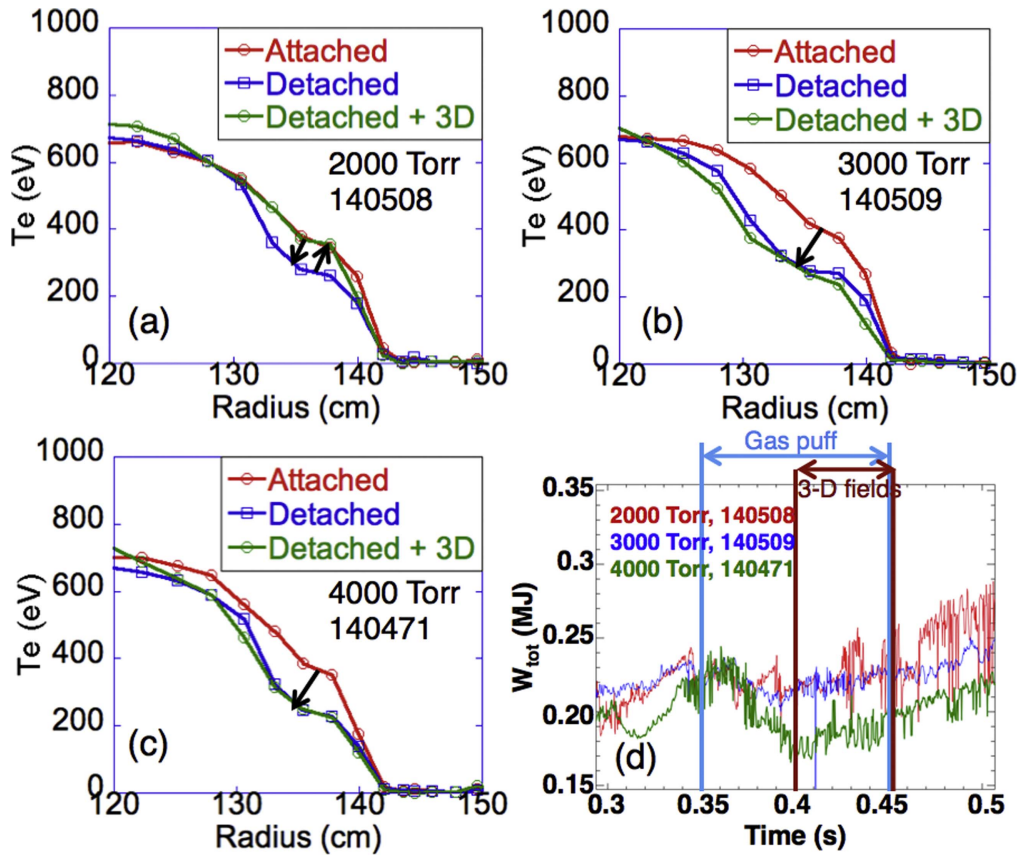
Figure 4. Change in electron temperature (T_e) profile and total stored energy (W_{tot}) over the time window of divertor gas puff and 3D field application for the NSTX discharges in figure 3. Plots (a)–(c) are for different amount of divertor gas puff, 2000 through 4000 Torr of gas pressure, respectively, and the green profile in plot (a) represents the re-attachment case induced by 3D fields. Plot (d) shows the temporal evolution of W_{tot} with gas puff and 3D field application during the discharges indicated in (a)–(c).

remains detached, would increase the far SOL heat flux level by at least 20%–30% compared to the axisymmetric detachment case. This can reduce the margin for the maximum surface temperature allowed for the safe machine operation. More gas puff to eliminate the far SOL striations would cause more confinement degradation, as seen in figure 4(d), and increase the possibility of the MARFE development and a subsequent radiative collapse of the plasma.

2.2. Effect of 3D fields on detachment in DIII-D

2.2.1. Setup and diagnostics. DIII-D has a total of 12 in-vessel 3D field coils, the 'I-coils', with half of them in the upper row and the other half in the lower row (see figure 7). Contrary to the single row, mid-plane coils in NSTX, the two rows of I-coil allows for tuning the alignment of the pitch of the magnetic perturbation with that of equilibrium fields. These coils can create magnetic perturbations with $n = 1, 2, 3$ toroidal mode number, but all RMP experiments for the investigation of the impact on divertor and detachment were done with $n = 3$. When the coils are configured such that the top and bottom pairs of coils produce fields that point in the same radial direction, they are termed to be in an 'even parity' configuration. When they produce fields in the opposite direction, it is called the 'odd parity' configuration.

The IR camera view, gas puff location, divertor Thomson scattering (DTS) chords, and target Langmuir probe (LP) arrays are also overlaid in the poloidal plasma cross section in figure 7. A set of bolometer arrays enables to obtain the poloidal distribution of the radiated power (P_{rad}) in the divertor area. Since the DTS chords are 1D, strike point sweeping is needed to obtain 2D divertor T_e and n_e data. Radial spacing of target LPs is 1.5–2.8 cm, so strike point sweeping is also necessary to obtain high-resolution profile of ion particle flux.

2.2.2. Experimental observation of the effect of 3D fields. Density pump-out typically occurs when the RMP is applied to low collisionality plasmas in DIII-D, while it is typically not observed for high collisionality plasmas [1, 2]. It is almost always accompanied by the increase (by a factor up to 2–3) of steady state, i.e. inter-ELM, peak heat flux, but this increase is largely removed when line average density is raised to the level before the RMP application. For the 3D detachment experiment, a series of density scan discharges were produced by puffing deuterium with both even and odd parity $n = 3$ RMPs applied [15–19]. Gas puffing was initiated a few 100 ms after turning on the RMP and was increased until the core density met and then exceeded the pre-RMP level. The plasma shape in figure 7 is the typical low triangularity shape
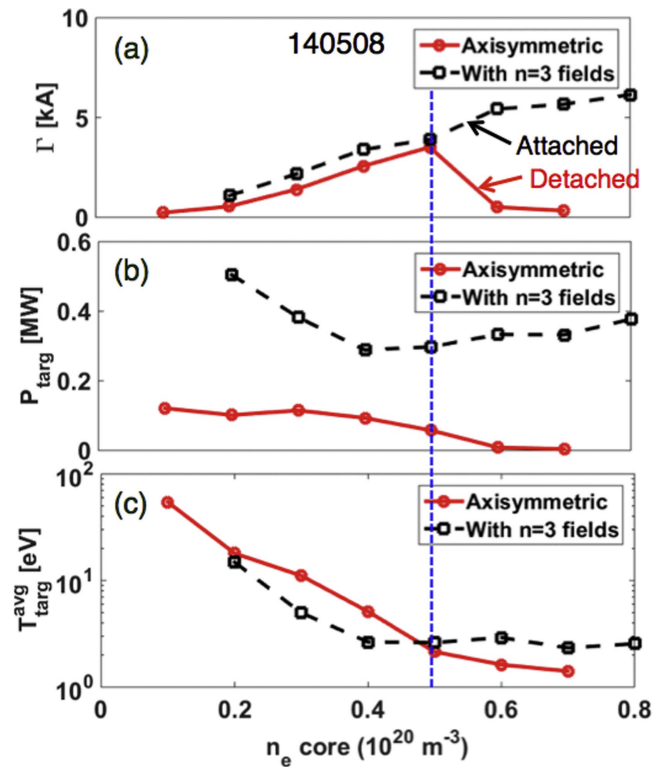
Figure 5. Comparison of ion particle flux (a), power to the divertor target (b), and the average electron temperature at the target (c) with (black dashed line) and without (red solid line) $n = 3$ fields, as a function of core electron density, from an EMC3-Eirene simulation for the same discharge as in figures 3(a)–(c) and 4(a) in NSTX. It is seen in plot (a) that an abrupt decrease of ion particle flux occurs at $n_e = 5 \times 10^{19}$ (m^{-3}) in case of no 3D fields, which is a typical indication of divertor detachment. This is compared to the continuous increase of particle flux when 3D fields were applied, i.e. the divertor plasma remained attached.

to allow better diagnostic measurements of the outer strike point (OSP).

Shown in figure 8 are the outer heat flux profiles measured during a series of density scan discharges for three cases; no RMP, $n = 3$ odd, and $n = 3$ even parities, where the densities in all three cases were matched [17]. These measurements were made by taking the average of multiple heat flux profiles during the inter-ELM period. Only a narrow toroidal section of lower divertor plates are covered at the ~60° toroidal position. The heat flux profiles show the typical exponential decay pattern in the near SOL (i.e. for $R - R_{sep} \sim 0.02\text{–}0.1$ m) with high q_{peak} at lower core density ($n_e/n_{GW} = 0.5\text{–}0.6$), as shown in figure 8(a), when no RMP is applied. The q_{peak} continues to decrease as the density is raised from $n_e/n_{GW} = 0.5$ to $n_e/n_{GW} = 0.8$. The radiated power is seen to move from the OSP toward the X-point at around $n_e/n_{GW} = 0.7$, an indication of detachment onset of the OSP; see figures 8(d) and (e). The q_{peak} is strongly reduced as the density is increased past the detachment onset into the higher density level. Application of RMP induces local peaks and valleys in the heat flux profile while the OSP is attached (i.e. for n_e/n_{GW} lower than ~0.7 for the discharges in figure 8), representing the lobe structures formed from the
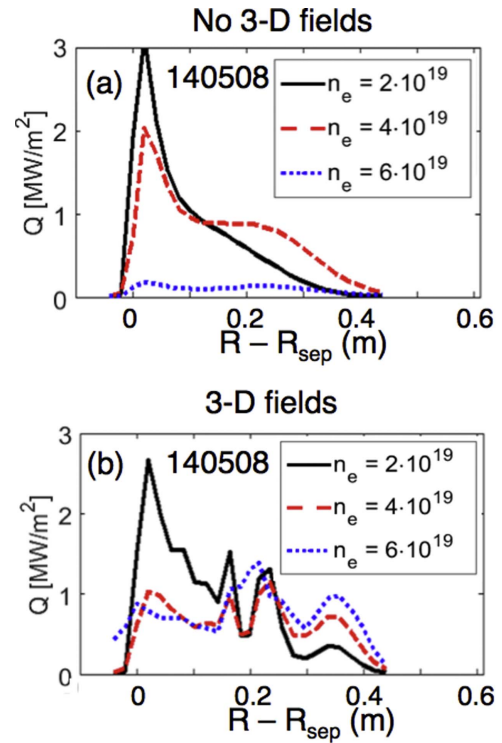

Figure 6. Heat flux profile simulated by EMC3-EIRENE for a density scan ($\bar{n}_e = 2\text{–}6 \times 10^{19}$ m^{-3}) without (a) and with (b) $n = 3$ perturbation fields applied, for the same discharge as in figures 3(a)–(c) and 4(a) in NSTX.

separatrix splitting. It is seen that the even parity RMP produces more pronounced lobe structures than the odd parity and accordingly the reduction of the q_{peak} is generally stronger for the same core density level, see figures 8(b) and (c) compared to 8(a). These asymmetries in heat flux begin to weaken as the plasma approaches detachment onset and finally disappear after the transition to detachment. Then the profiles become almost identical for the no RMP case and either the even or odd parity case [17]; see the profile for $n_e/n_{GW} \sim 0.8$ in each case in figure 8. The transition threshold, $n_e/n_{GW} \sim 0.7$, is very similar for all three cases, i.e. the RMP did not alter the onset threshold for these discharges. It is also found that the electron temperature and density profiles across the whole plasma cross section, measured by Thomson scattering, have not been changed by the RMP [17].

The behavior of divertor target heat flux profiles as a function of the core density (n_e/n_{GW}) is also demonstrated in figure 9, where the total integral power $\left(P_{targ} = \int 2\pi r q(r) \mathrm{d}r\right)$, peak heat flux ($q_{peak}$), and the wetted area ($A_{wet} = P_{targ}/q_{peak}$) are plotted as a function of the Greenwald fraction for the three cases; no RMP (black), the $n = 3$ odd parity (red), and the $n = 3$ even parity (green). It is seen that the total integral power is largely unchanged for all three cases in the range of n_e/n_{GW} investigated, see figure 9(a). However, the inferred A_{wet} increases noticeably in the attached condition ($n_e/n_{GW} < 0.7$) when the RMPs are applied, which leads to the reduction of the q_{peak} compared to the no RMP case, see figures 9(b) and (c).
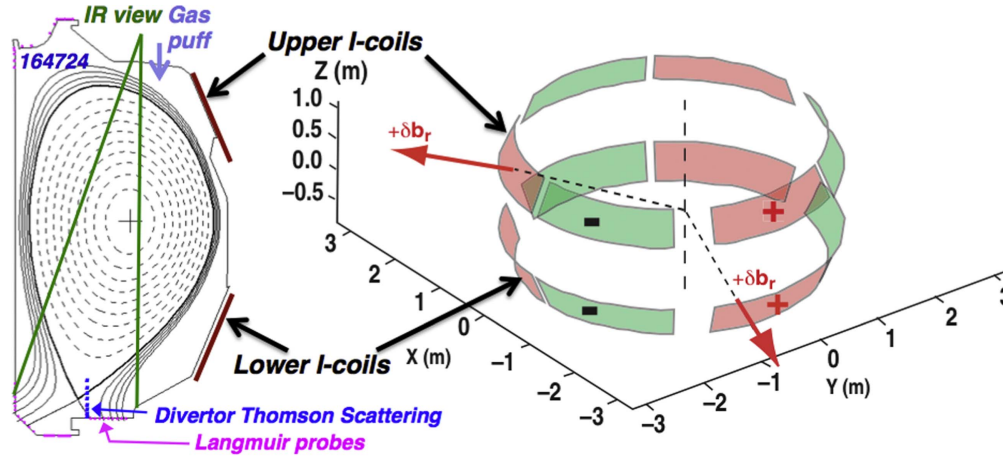
Figure 7. Poloidal cross section of a DIII-D plasma with upper and lower I-coils, IR camera view, gas puff location, divertor Thomson scattering (DTS) chords, and the target Langmuir probe arrays overlaid. The right plot shows the bird's eye view of I-coils (six coils for each of upper and lower row).

Note that although the A_{wet} was deduced from the P_{targ} and the q_{peak} from the above relation, it reflects how P_{targ} is spatially dispersed to the divertor target and determines the q_{peak}. It is noted that the heat flux spreading effect in the clear attachment case (for $n_e/n_{GW} < 0.6$) is stronger, i.e. higher A_{wet} and lower q_{peak}, for the even parity configuration than the odd, which appears correlated with the more pronounced lobe heat flux for the even parity (figure 8(c)) than the odd (figure 8(b)). The A_{wet} and q_{peak} discrepancy for the three cases is large for the low n_e/n_{GW}, then becomes smaller for higher n_e/n_{GW}, until all three A_{wet} and q_{peak} values become nearly identical in the detached case. Along with the unchanged detachment onset condition ($n_e/n_{GW} \sim 0.7$) compared to the no RMP case, this indicates that the RMP effect on the divertor heat flux characteristics diminishes as approaching the detached condition for this series of discharges. Earlier work [15, 16] also showed similar results and this is in contrast to the NSTX data that shows strong effect of 3D fields on detachment under certain conditions, such as the re-attachment of divertor plasma and the generation of clear heat flux striations as seen in figures 3(c) and (f).

Contrary to the cases shown in figures 8 and 9, the two high-density cases (with and without RMP) in figure 10 from a different series of discharges show evidence that the RMP prevented detachment onset in cases where no RMP led to detachment for the OSP [18, 19]. Figures 10(a) and (b) show the radiated power near the X-point, measured by the imaging bolometer, is significantly lower in the case of RMP application ($n = 3$ even) compared to the no RMP case, even though the Greenwald fraction is slightly higher ($n_e/n_{GW} = 0.75$ versus 0.7). Accordingly, the heat flux profile for the RMP case is peaked near the OSP with the q_{peak} more than a factor 2 higher than that for the no RMP case, see figure 10(c). This indicates that the OSP is still attached in the presence of RMP even with the higher Greenwald fraction. Recent work [18, 19] also showed that the ion saturation current density (J_{sat}) profile, measured by target LPs, near the OSP is strongly reduced (a characteristic of detachment) only in the no RMP case, while the J_{sat} profile with the RMP reveals a peak near the OSP (a characteristic of

the high recycling regime), for the same discharges shown in figure 10. Evidence that detachment does not onset at this density also originates from the DTS T_e data [18, 19], where the T_e at the divertor surface for the no RMP case is well below 5 eV for the whole divertor area from the OSP but for the RMP case it still is $\sim$10 eV near the separatrix. Although the secondary T_e lobe move away from the target, the lobe structure still remains even with the higher Greenwald fraction compared to the no RMP case. The observation that the plasma did not enter detachment with the RMP even at a higher density than in the no RMP case is similar to the re-attachment by the applied 3D fields seen in NSTX as described in section 2.1.2 (figure 3(c)).

Understanding of the cause that makes the difference in the effect of RMP on detachment between the cases shown in figures 8, 9 and figure 10 is still in progress, but it is found that [18, 19] the core T_e is higher with the RMP, while n_e is similar, for the case of no detachment transition (figure 10). The higher core T_e is correlated with the suppression of a rotating MHD mode ($n = 2$), detected by magnetics, by the RMP. It is seen in figure 10(d) that this mode only appears after the RMP is turned off for the RMP discharge (red trace), and was sustained for the whole period of detachment for the no RMP case (black trace). In contrast, for the case of the same onset threshold (figures 8 and 9), the T_e profile remained unchanged with the RMP and no suppression of MHD mode by the RMP was observed. However, it is not clear yet how the RMP eliminated the MHD mode and this needs further investigation.

2.2.3. EMC3-EIRENE simulation result. A series of EMC3-EIRENE simulations for an upstream density scan was performed and the result was compared to measurements [18, 19]. In the lower density calculations, the lobes in the electron temperature in the divertor extend to the target plate. This structure is qualitatively similar to the experimental lobe structure seen in the DTS data described in section 2.2.2. As the upstream density in the simulation is increased the lobes in the electron temperature are cooled near the target plate.
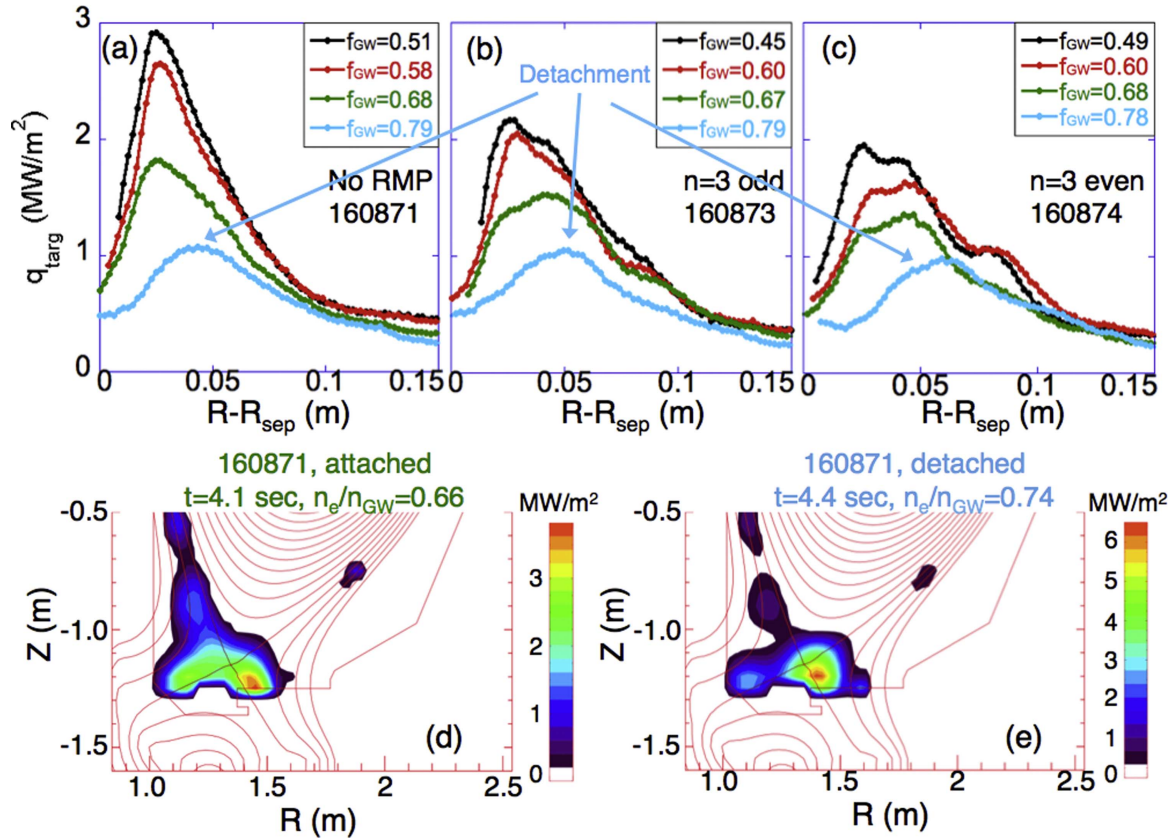
Figure 8. Measured divertor heat flux profiles with the increase of core density in DIII-D, as a function of the radial distance relative to the location of outer strike point ($R - R_{sep}$). (a) is without the RMP, (b) is with the $n = 3$ odd RMP applied, and (c) is with the $n = 3$ even RMP. The Greenwald fraction ($f_{GW} = n_e / n_{GW}$) is used as a metric for the core density level for each case. The profile in sky blue ($f_{GW} \sim 0.8$) for all three plots shows the case for divertor detachment. Plots (d) and (e) show the poloidal distribution of radiated power density (P_{rad}) measured by a bolometer array for $f_{GW} = 0.66$ (attached condition) and 0.74 (detached), respectively, for the no-RMP case. Note that the behavior of P_{rad} as a function of f_{GW} is very similar for all three cases.

This structure change is also qualitatively similar to that seen in the DTS measurement. In these simulations the magnetic field structure and perpendicular transport coefficients were held constant and only the density at the upstream boundary was varied. Here, the vacuum model for the 3D magnetic field structure was used, which does not include plasma response fields to the RMP. By holding the magnetic field structure constant these calculations demonstrate that changes in magnetic field structure are not needed to explain the changes in the electron temperature within the divertor. From the simulated divertor T_e and n_e data at the divertor surface, the 2D target heat flux profile is calculated and compared to the experiment.

Figure 11 illustrates a comparison of simulated heat flux profiles for the low and high density cases to the measured profiles, both with the $n = 3$ even parity RMP. The 1D profile from the EMC3-EIRENE simulation is the radial cut at the toroidal location of the IR camera from the 2D target heat flux data in the (r, ϕ) plane. It is seen that the peak heat flux decreases and the lobe structure in the simulated heat flux profile becomes much less pronounced with the increase of density; figure 11(a). Experimental profiles show similar trend, figure 11(b), although the lobes are less distinct compared to the simulated profile for the low density case.

This difference indicates that the $\chi_\perp / \chi_\parallel$ ratio used in the simulation may have been lower than in the experiment. Overall, the agreement is quite good in terms of the location of the lobes and the trend of heat flux behavior with the density increase.

Recent calculations with various plasma response models used for *B*-field structure, e.g. ideal (IPEC) and resistive (M3D-C1) model, showed that no *B*-field model tested can explain pedestal and divertor data simultaneously when tested on multiple perturbation coil configurations [24]. For example, vacuum fields show too much stochasticity inside the separatrix, while ideal MHD solution reproduces the experimentally observed pedestal gradient in the steep region but it becomes too flat near the separatrix. On the other hand, strong screening from M3D-C1 removes downstream lobes and the result is sensitive to the edge rotation.

3. Effect of 3D fields on detachment in stellarator (LHD)

Magnetic configuration in stellarator is inherently non-axisymmetric and its magnetic field geometry is thought to play
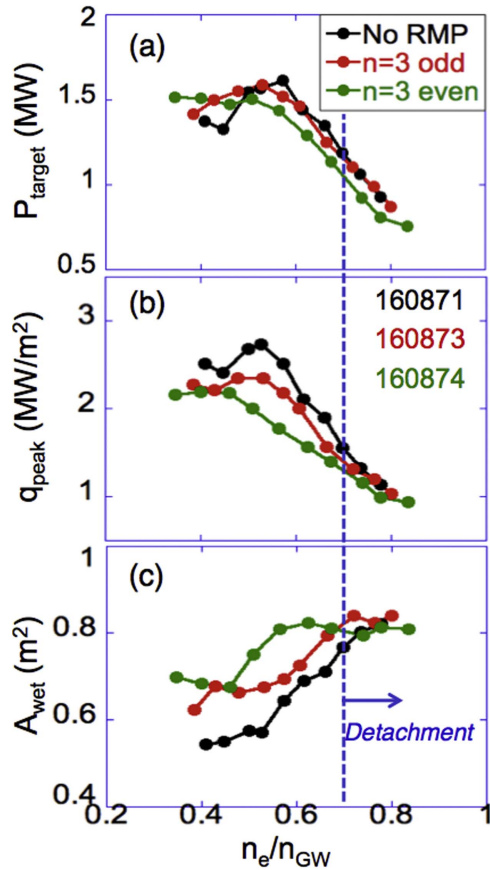
Figure 9. Behavior of outer divertor heat flux profiles as a function of Greenwald fraction in DIII-D with no RMP (black), the $n = 3$ odd RMP (red), and the $n = 3$ even RMP (green) applied. Plot (a) is the total integral power (P_{target}) calculated from the heat flux profile, (b) is the peak heat flux (q_{peak}), and (c) is the wetted area ($A_{\text{wet}} = P_{\text{target}}/q_{\text{peak}}$) of the profile. Divertor detachment onset was at the Greenwald fraction of ~0.7, regardless of whether the RMPs were applied or not for this series of discharges; see figures 8(d) and (e).

an important role for stability of radiative/detached plasma because of the strong anisotropy of energy transport with respect to magnetic field vectors. Contrary to the results in tokamaks that show an increase of detachment onset threshold in the presence of 3D fields [13, 14, 17, 18, 23, 24], there are reports that detached operations become more stable in stellarator under certain conditions, when the existing 3D edge magnetic field structure is further modified by additional external coils to produce pitch resonant fields leading to the formation of tearing islands on rational surfaces [25–30]. The additional 3D fields in stellarator change the rotational transform ($\iota = 1/q$) profile therefore the internal pitch of local fields. This directly changes the perpendicular to parallel transport ratio and affects the divertor density regime. So the RMP provides more flexibility for the control and optimization of the divertor operation even in the 3D helical devices. Extensive work for the stabilization effect on detached operation was conducted in LHD in recent years [25–28, 37, 38] and the main findings in both experiment and simulation will be reviewed in this section.

3.1. Magnetic field structure with RMP

A bird's eye view of LHD's superconducting helical coils and RMP coils, along with plasma shape is provided in figure 12(a). The magnetic field is produced by superconducting coils with a poloidal winding number of $l = 2$ and toroidal field periods of $n = 10$. Due to the mode spectrum of magnetic field produced by the helical coils, magnetic islands of different mode numbers are created, and they overlap each other. This creates an intrinsically stochastic field line structure in the edge region. The RMP coils installed at the top and bottom of the machine produce $n/m = 1/1$ RMP fields, which have a resonance layer ($\iota = n/m = 1$) in the stochastic region and create remnant islands. The radial profile of the rotational transform is plotted in figure 12(b) with and without RMP fields. Figure 12(c) shows connection length (L_c) distribution at the edge of LHD plasma. The stochastic field lines are characterized by long connection length (>100 m), while remnant islands also exist due to incomplete island overlapping. The region consisting of long L_c field lines with remnant islands is called the stochastic region, while the outermost region consisting of a mixture of long and short L_c field lines is called laminar region or edge surface layers [52]. The lower half of figure 12(c) shows L_c distribution with the RMP fields.

3.2. Stabilization effect of RMP on detached operation

Figure 13 shows the time trace of plasma parameters obtained in a sustained detachment discharge with $n/m = 1/1$ RMP fields (red), in comparison with no RMP case (blue). The RMP was applied before the discharge initiation and was kept on throughout the discharge. In both cases, density was ramped up by gradual gas puff. The radiated power and divertor heat flux, figures 13(b) and (c), was estimated respectively from photodiode array and target LP data. Without RMP, the radiated power first increases gradually with increasing density but the rapid increase from $t \sim 3.8$ s indicates onset of a thermal instability. The instability grows so fast that it leads to discharge termination. With the RMP, however, the transition to an enhanced radiation state occurs at $t \sim 3$ s, and it leads to divertor heat flux reduction by a factor of 3–10. The detached operation is successfully sustained by gas puff feedback control up to the end of the neutral beam injection. During the detached phase, the divertor T_e decreases to ~5 eV and the divertor particle flux profile at the inboard side becomes flat with a significant reduction in peak values [25]. These results show stabilization effect of the RMP on the radiating edge plasma. Investigation of toroidal profiles of divertor particle flux using the probe arrays in 10 toroidal sections shows that there is $n = 1$ mode structure. It is also found that particle flux in most of the sections decreased at the detachment transition, although flux for one section even increased. The total flux averaged over all sections was reduced after the detachment onset. Radial profiles of T_e, n_e, and carbon radiation intensity are also shown in figure 13. The radiated power of carbon was estimated by assuming $n_{\text{carbon}} = 0.01 n_e$ and $n_e \tau = 10^{17}$ m^{-3} s.

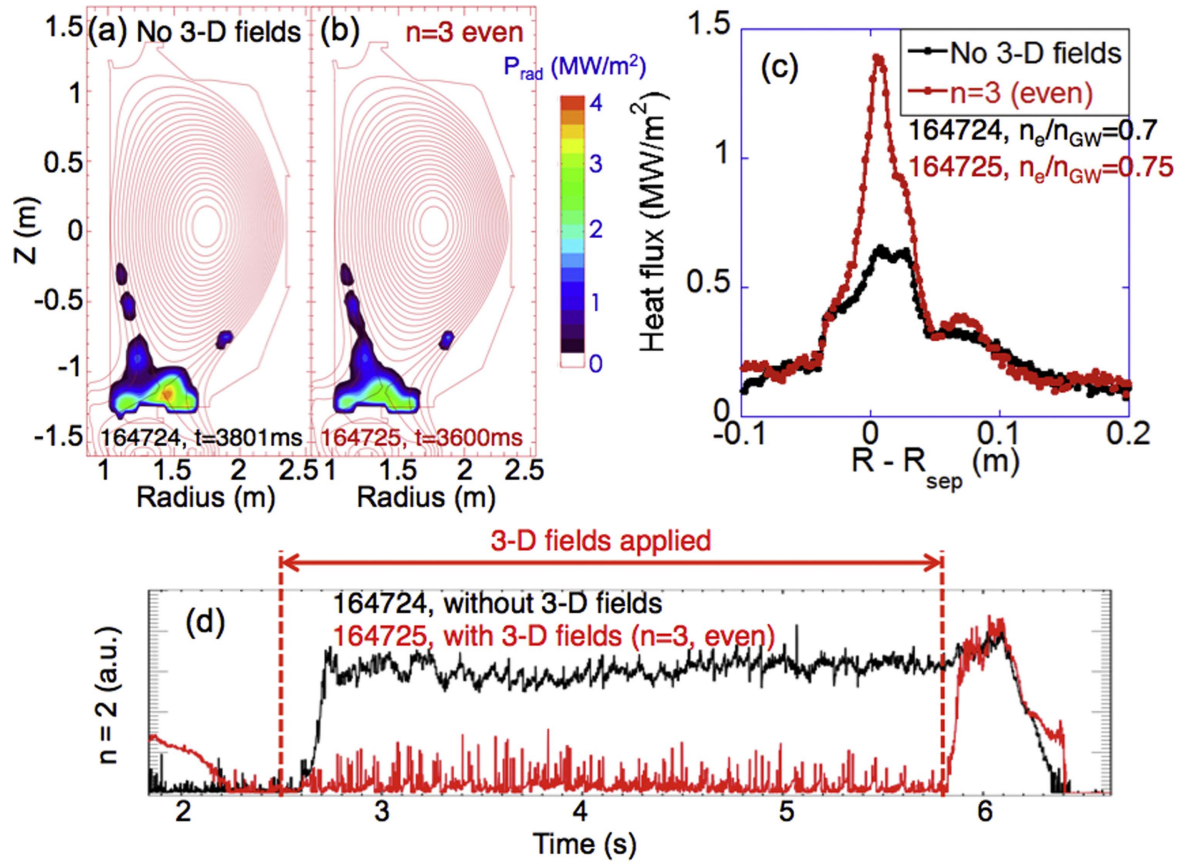**Figure 10.** Plots (a) and (b) are poloidal images of measured radiated power in two high density ($f_{GW} > 0.7$) discharges in DIII-D. Plot (a) is the case without RMP and (b) is with the $n = 3$ even RMP applied. Plot (c) shows a comparison of measured divertor heat flux profiles respective to the case (a) and (b). Plot (d) is a trace of $n = 2$ MHD mode amplitude measured by magnetics without and with RMP.
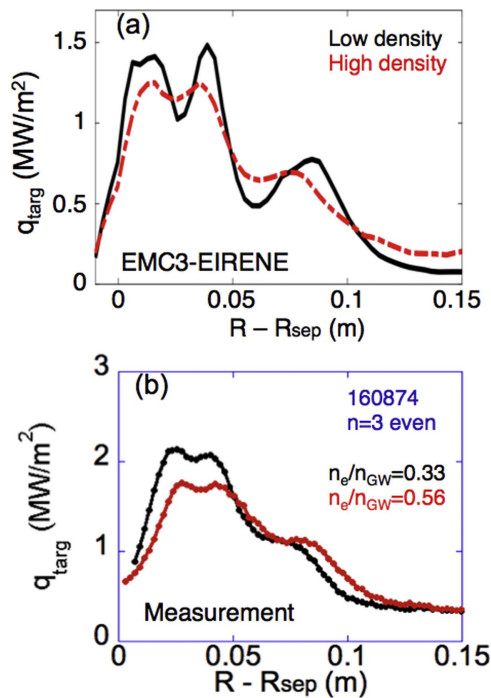

Figure 11. Divertor target heat flux profiles with the $n = 3$ even parity RMP in DIII-D for low (black) and high (red) density cases. Plot (a) is from an EMC3-EIRENE simulation and (b) is the measured profiles.

Flattening of T_e in the resonance layer is clearly seen in figure 13(f) while n_e profile remains largely unchanged. Due to the temperature dependence of radiative loss function of carbon, the drop in T_e enhances the calculated carbon radiation power in the resonance layer (figure 13(h)), which is consistent with the rise of measured radiation power after the transition to detached divertor, as shown in 12(b). The RMP-assisted detached operation was also combined with neon impurity seeding successfully in LHD, which further enhanced radiation power and reduced divertor particle flux [53].

Another notable feature of the RMP-assisted detached divertor is the recovery of plasma stored energy, see figure 13(e). This is attributed to the pressure peaking in the core region after the transition to detached divertor [25, 27]. This is in sharp contrast to the behavior of conventional radiative/detached divertor in tokamaks with an X-point, where significant confinement degradation is almost always observed due to the penetration of a radiation front into the core region.

3.3. Modification of 3D radiation distribution by RMP

An EMC3-Eirene simulation revealed the spatial structure of radiation distribution with and without RMP; carbon radiation distributions in the poloidal cross section at a specific toroidal
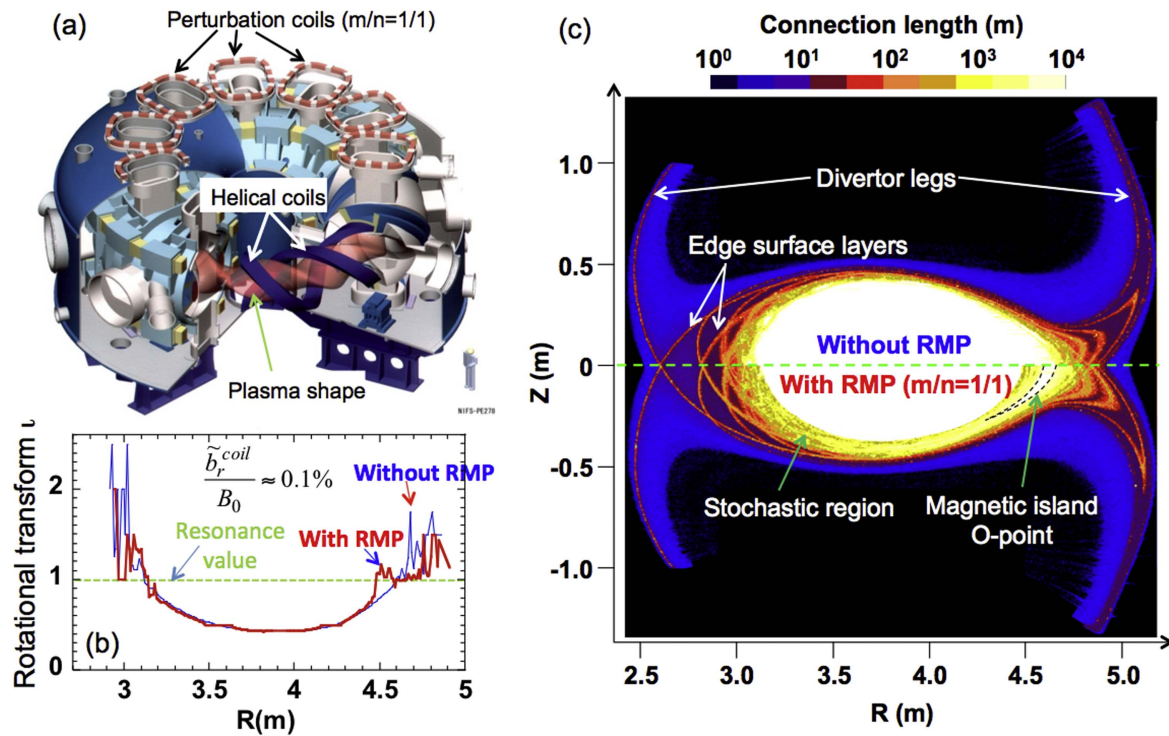
Figure 12. (a) A bird's eye view of helical coils, magnetic perturbation coils, and the plasma shape in LHD. (b) Rotational transform ($\iota = 1/q$) profile with (blue) and without (red) the RMP. (c) Poloidal cross section of connection length (L_c) distribution for a horizontally elongated section with (lower half) and without (upper half) the RMP. The applied RMP creates remnant islands in the stochastic region with O-point located at the outboard side in this cross section. The divertor legs are stretched from the in- and outboard sides towards the divertor plates. Reproduced courtesy of IAEA. Figure from [25]. Copyright (2013) IAEA.

angle $\varphi = 93°$, are shown in figures 14(a) and (c). The simulation also shows that the fraction of carbon radiation in P_{SOL} is 40% without RMP and 60% with RMP. Here, P_{SOL} is defined as the total power leaving the main plasma across the LCFS, some of which is radiated and the rest arrives at the surface of plasma facing components.

Figure 14(a) shows that radiation is peaked on the inboard side and is maintained in the edge region when there is no RMP. However, the radiation front penetrates into the core plasma when the density is raised, which ultimately collapses the plasma. This simulation result is experimentally supported by the infrared video bolometer measurements in the radiation collapse phase and showed qualitatively similar poloidal distribution [25]. On the other hand, figure 14(c) illustrates that the RMP moved the peaking of radiation to the bottom of the plasma. This is where the X-point of $n/m = 1/1$ island is located and thus the interpretation is that the RMP induces cooling only around the island X-point. It is thought that the isolation of flux tubes around the X-point causes the localized cooling due to the singularity in the field line geometry. Perpendicular transport, much smaller than the parallel transport, must be consequently responsible for most heat flowing to the X-point. This is why the decrease of temperature is larger for the X-point than other poloidal locations. The drop of temperature increases carbon radiation as the density is raised. This explains the move of radiation belt by RMP shown in figure 14(c).

Figures 14(b) and (d) show the radiation distribution in the toroidal and poloidal plane for the $\iota = n/m = 1$ resonant

surface, without and with RMP, respectively. Note that $0°$ in the poloidal direction is for the outboard side and $180°$ is for the inboard side. For no RMP case, figure 14(b), the radiation is strongly peaked at the inboard-side with 10 toroidal periods, which reflects the 10 periods of magnetic fields from the LHD coil configuration. The mode structure of remnant islands in the stochastic layers modifies flux tubes poloidally, thus the fine structure of radiation pattern is extended also in the poloidal direction. For the RMP case, figure 14(d), the trajectory of $n/m = 1/1$ island X-point created by RMP modulates the pattern of radiation peaking. The radiation peaking on the inboard side near the X-point of $n/m=1/1$ island is still observed for $\varphi = 130°$–$230°$, but the toroidally uniform characteristic for the radiation pattern seen in figure 14(b) no longer exists. This is due to the breaking of toroidal symmetry by RMP fields.

The simulated radiation distribution with and without RMP fields was compared to the measured radiation profile with reasonable agreement in the global distribution pattern. It is thought that the modified field structure created by the RMP holds the radiation belt near the X-point of 1/1 island preventing it from penetrating inward.

3.4. Role of plasma response in RMP-assisted detached operation

Magnetic fields generated inside the plasma in response to the applied RMP fields have been estimated by magnetic diagnostics during the RMP-assisted detached operation experiments
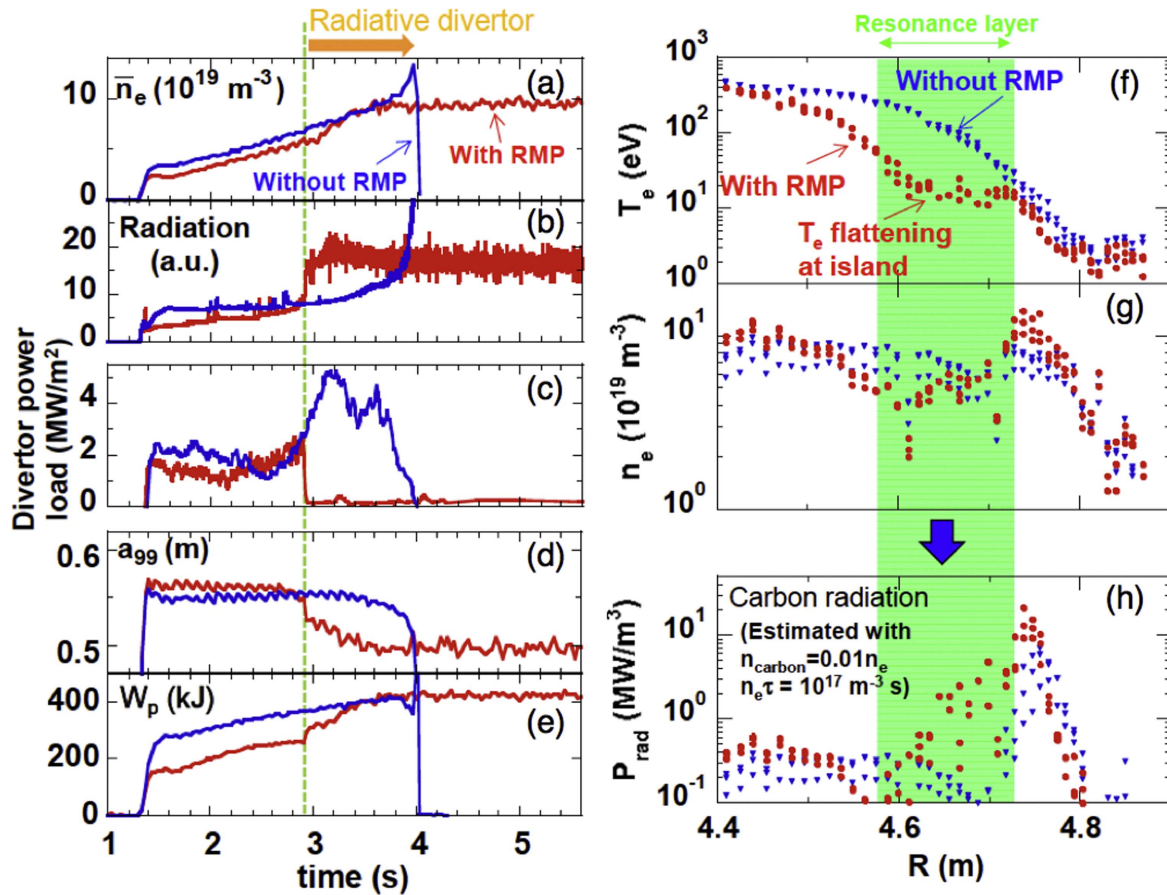
Figure 13. Time trace of (a) line average density, (b) radiation power, (c) divertor heat flux, (d) plasma minor radius containing 99% of total energy, and (e) total stored energy, with (red) and without (blue) RMP in LHD. Right plots show radial profiles of (f) electron temperature, (g) electron density, and (h) the carbon radiation intensity, with (red circles) and without (blue triangles) RMP. Plots (f)–(h) were reproduced courtesy of IAEA. Figure from [25]. Copyright (2013) IAEA.

[25, 37, 38]. Figure 15 shows the result of an RMP ramp-up experiment with density maintained almost constant. It is found that the poloidal phase of plasma response fields with respect to that of RMP fields, θ_r^{plasma}, is closely related to the stable transition to detached regime. During the ramp-up of RMP coil current, a transition to detached regime occurs when the radial component of RMP fields (b_r^{coil}) exceeds 0.07%–0.08% of *B*-field at the magnetic axis (B_0); see figure 15. A rapid change in θ_r^{plasma}, from 1π toward 0 radian, is observed at the time of transition to detachment. Note that $\theta_r^{plasma} = \pi$ means that the response fields are out of phase relative to the RMP fields, leading to cancellation of RMP fields, therefore healing of $m/n = 1/1$ island is expected. $\theta_r^{plasma} = 0$ indicates that plasma response is in-phase with RMP and thus it enhances RMP fields, which leads to the growth of island. This interpretation is supported by the flat T_e profile in the resonance layer in case of RMP, shown in figure 13(f), indicating the existence of island. More detailed investigation of plasma response in LHD [37, 38] show that θ_r^{plasma} should be lower than a critical value ($\sim 0.32\pi$) in order for the RMP to induce transition to stable detachment. This critical value is not affected by either collisionality or plasma β [37]. It is interesting that the clear role of plasma response in the magnetic island growth in LHD, which appears to stop the radiation belt from penetrating into the core plasma

and lead to the stabilization of detachment, is not observed in tokamaks. The high edge rotation speed in the tokamak H-mode plasmas that could screen the RMP fields might be the reason why the island growth does not occur, therefore no detachment stabilization, in tokamaks.

4. Comparison of 2D and 3D detachment

4.1. Stellarator and limiter tokamaks

Divertor detachment is achieved via pressure loss along the flux tube, but the underlying processes are different between 2D and 3D configurations. In the 2D axisymmetric geometry, the increase of upstream density such that the mean free path for collisions becomes smaller than the connection length (L_c) leads conduction to play an important role. This is the 'high recycling regime', where the T_e and n_e gradient is developed along the flux tube but pressure is conserved along *B*-field and there's no momentum loss. A further increase of density spreads power over a larger area via increased radiation near the X-point and then the divertor plasma finally reaches the 'detached regime' when charge exchange (CX) dominates over ionization. In this situation, hot neutrals remove momentum and energy from the plasma leading to pressure
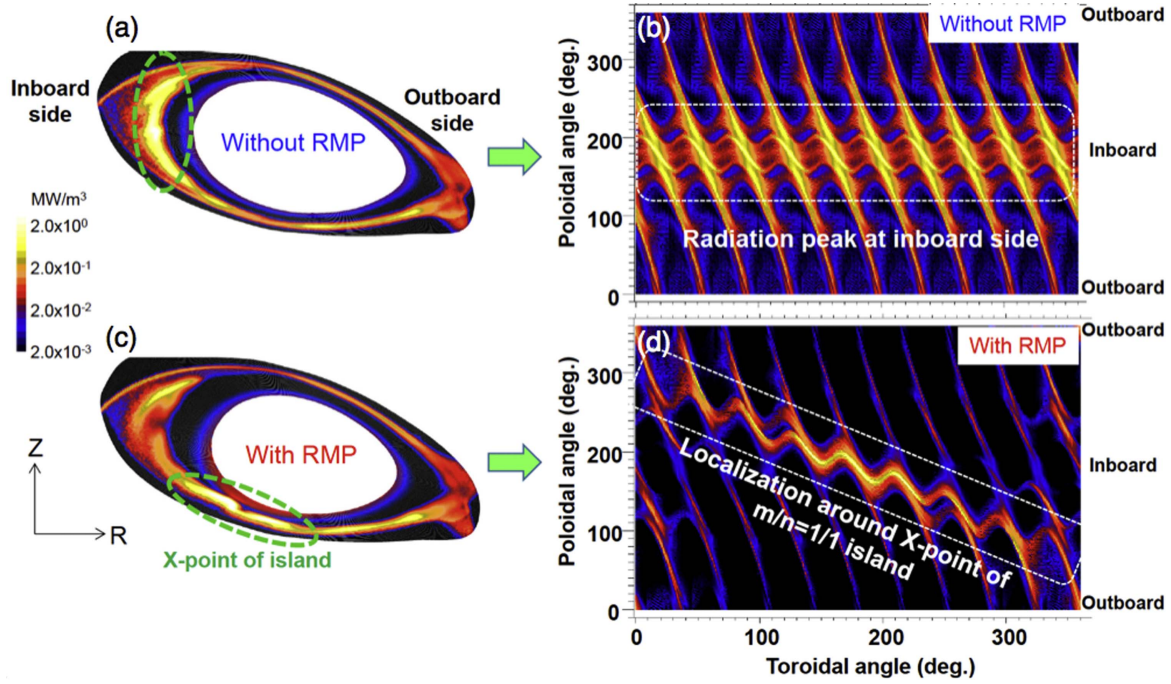
Figure 14. Carbon radiation distribution, calculated from an EMC3-Eirene simulation, without (upper plots) and with (lower ones) RMP for the case shown in figure 13. Left plots are poloidal cross section of radiation power at toroidal angle (φ) = 93°, and right plots are radiation distribution in the plane of toroidal and poloidal angle. Reproduced courtesy of IAEA. Figure from [25]. Copyright (2013) IAEA.
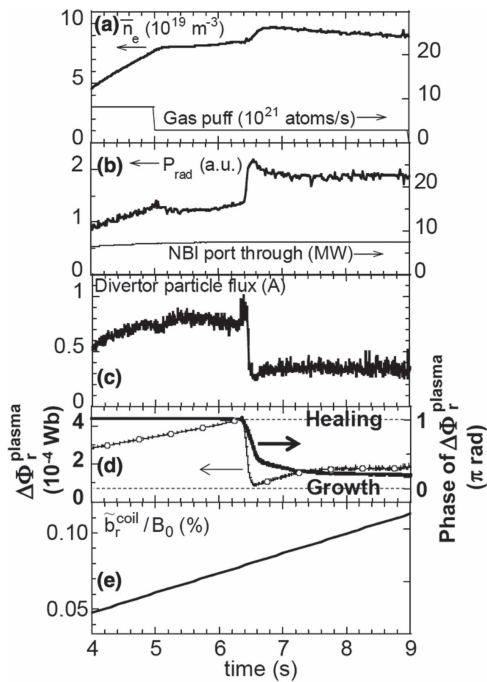

Figure 15. Time trace of (a) line average density, (b) radiated power, (c) divertor particle flux measured by LP, (d) phase of the plasma response fields relative to the RMP fields, θ_r^{plasma} (solid line), and amplitude, $\Delta\Phi_r^{plasma}$ (dotted line with open circles), and (e) the strength of RMP fields during an RMP coil current ramp-up experiment in LHD. The transition to detachment occurred at $t = 6.5$ s.

loss. The plasma at the target becomes so cold that the ionization region ($\sim$5 eV) 'detaches' from the divertor plate moving some distance upstream. Therefore, both the heat and particle flux to the target is dramatically reduced. The

pressure conservation along the flux tube in high recycling regime gives rise to strong dependence of target density and temperature on the upstream density that has been confirmed experimentally [54, 55]; $n_{target} \propto n_{up}^3$ and $T_{target} \propto n_{up}^{-2}$.

However, the absence of a high recycling regime prior to detachment has been observed in 3D configurations including stellarators and limiter tokamaks with RMP, e.g. W7-AS [56, 57], LHD [58], and TEXTOR [59]. There are two contributing factors to this phenomenon. The first one is the enhanced momentum loss caused by counter-streaming flows in the 3D configuration. Figure 16 shows that neighboring channels of opposite flows in the island divertor in stellarators can approach to each other or even partially overlap, which leads to perpendicular loss of parallel momentum. The resulting friction force (via perpendicular viscosity) has to be balanced by the pressure gradient force that increases up/down pressure ratio consequently, i.e. detachment. Note that the pressure loss here is not due to the CX process as in the 2D detachment but is purely caused by 3D geometric effect. Therefore detachment onset occurs before the divertor plasma enters high recycling regime with $T_{target} \gtrsim 10$ eV. The experimentally revealed dependence of n_{target} and T_{target} on n_{up} is indeed much weaker than in the 2D detachment case [57–59]; $n_{target} \propto n_{up}^{\tilde{1}}$ and $T_{target} \propto n_{up}^{\tilde{-1}}$. The second factor is the ratio of perpendicular to parallel heat transport ($q_{\perp e}/q_{\parallel e}$) in the SOL and divertor. Reduction of parallel electron heat conduction ($q_{\parallel e}$) due to the increase of perpendicular heat transport ($q_{\perp e}$) or parallel heat convection ($q_{\parallel conv}$) increases this ratio, which consequently reduces the parallel temperature gradient and thus leads to the absence of high recycling regime and the early transition to detachment. It is shown
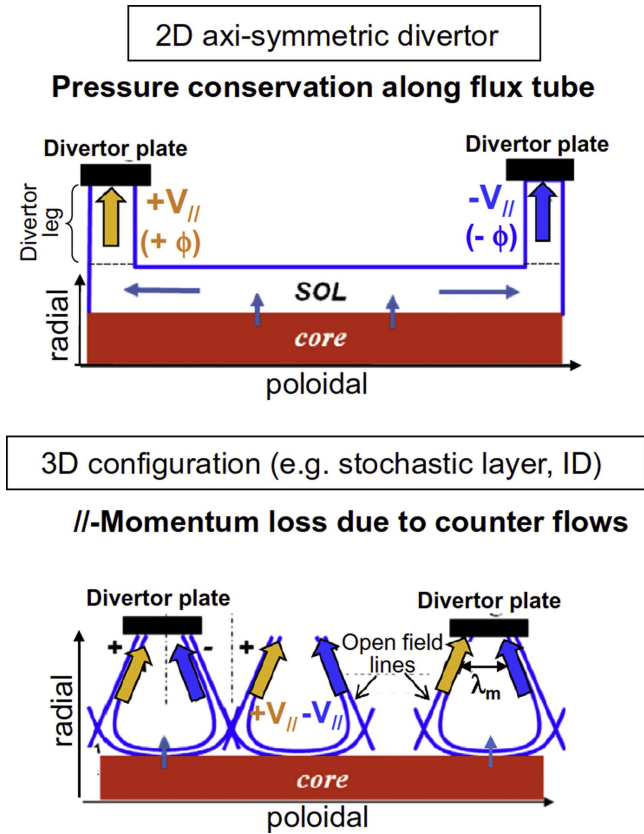
Figure 16. Schematic diagram of parallel flow to divertor plates in single null poloidal divertor in a 2D tokamak (upper plot) and in a 3D divertor configuration (lower). It is seen that opposite ion flows in the inner and outer divertor legs are isolated from each other in terms of perpendicular transport in the 2D tokamak case. In the 3D configuration, neighboring channels of counter flows approach to each other and can enhance loss of parallel momentum via perpendicular viscosity. Reproduced courtesy of IAEA. Figure from [28]. Copyright (2015) IAEA.

numerically in TEXTOR [51] that this effect can be large to induce detachment without entering high recycling regime even with no significant momentum loss from the friction between counter-flows.

Under certain conditions, the recovery of high recycling regime in 3D configuration was found in several machines such as TEXTOR [60], Tore Supra [61], and W7-X (numerical simulation) [57]. For example, the momentum loss effect can be small if the geometric separation of counter flow is large enough. Also, high upstream T_e (e.g. in high input power) in the SOL can greatly increase parallel heat conduction ($q_{\parallel e} \propto T_e^{5/2}$), leading to small $q_{\perp e}/q_{\parallel e}$ and the restoration of high recycling regime. Figure 17 shows two examples from TEXTOR Dynamic Ergodic Divertor (DED) experiments. Figure 17(a) illustrates the absence of high recycling regime in the $m/n = 6/2$ configuration [59], i.e. electron density (temperature) at the divertor target increases (decreases) linearly with the upstream density ($n_{e,target} \propto n_{e,up}^{\sim 1}$ and $T_{e,target} \propto n_{e,up}^{\sim -1}$) for the whole range of density ramp ($n_{e,up} = 1.2$–3.2×10^{19} m^{-3}). It is seen that $T_{e,target}$ is >20 eV when the ion particle flux begins to roll over (typical sign of detachment onset) at $n_{e,up} = 2.8 \times 10^{19}$ m^{-3}.

On the other hand, figure 17(b) demonstrates characteristics of clear high recycling regime for $n_{e,up} = 1.8$–2.8×10^{19} m^{-3}, i.e. target electron density (temperature) increases (decreases) with the upstream density much faster than linearly ($n_{e,target} \propto n_{e,up}^{4.2}$ and $T_{e,target} \propto n_{e,up}^{-1.8}$) in the $m/n = 3/1$ configuration [60]. Note that $T_{e,target}$ at the detachment onset at $n_{e,up} \sim 2.8 \times 10^{19}$ m^{-3} is still too high (>10 eV) for volume recombination to be the main process for detachment, indicating that the underlying physical mechanisms are not the same as in the conventional detachment.

4.2. X-point poloidal divertor tokamaks

H-mode plasmas in the divertor configuration have high toroidal rotation speed (V_t) in the edge region compared to L-mode. It is thought that high V_t can screen applied RMP more effectively to prevent stochastic layer and magnetic islands from forming inside the separatrix. One can expect that the 3D effect on the divertor density regime and detachment described in section 4.1 is likely to be less pronounced in this situation. For example, T_e flattening, an indicative of island formation, by the RMP in H-mode, diverted plasmas has not been observed in DIII-D, while clear island flattening in T_e at $m = 2, 3, 4$ was observed for $n = 1$ application in inner wall limited L-mode plasmas [62, 63]. Also, the X-point divertor configuration enhances parallel transport in the SOL compared to the limiter configuration, thus the effect of increased perpendicular transport by RMP becomes weaker. In fact, the momentum loss effect from the counter-streaming flow has not been observed experimentally in H-mode plasmas in any divertor tokamak thus far.

Numerical simulations using EMC3-EIRENE for H-mode plasmas in divertor tokamaks have been recently performed including DIII-D [64] and ITER [65, 66], where it is revealed that application of RMPs to axisymmetric X-point poloidal divertor configuration can generate counter-streaming parallel flow in the X-point region and at the divertor surface. Figure 18 is an example for ITER and a poloidal reversal of parallel flow direction, i.e. change of sign of Mach number, is seen in both vacuum and screened RMP case. In the region inside the orginal separatrix near the X-point, flow channels with poloidally and radially alternating flow direction are found to be generated by RMP with a checkerboard like pattern, figures 18(b) and (c). These counter flows are seen also for the inner and outer divertor lobes for the vacuum RMP case, but in the screened RMP case they are modified to strong and weak flow in the same direction closer to the divertor surface. This demonstrates that the plasma response can play an important role in setting parallel flow pattern. Even though screening effect is weak so strong counter flow is possible as shown in figure 18(b), it is not clear if the momentum loss effect would be large enough to facilitate detachment because the parallel transport is still dominant in tokamaks with the RMP, i.e. $q_{\perp e}/q_{\parallel e} \ll 1$. However, this at least leads to effective particle outflow from the pedestal region, which is consistent with the density pump-out observed in today's RMP experiments in tokamaks.
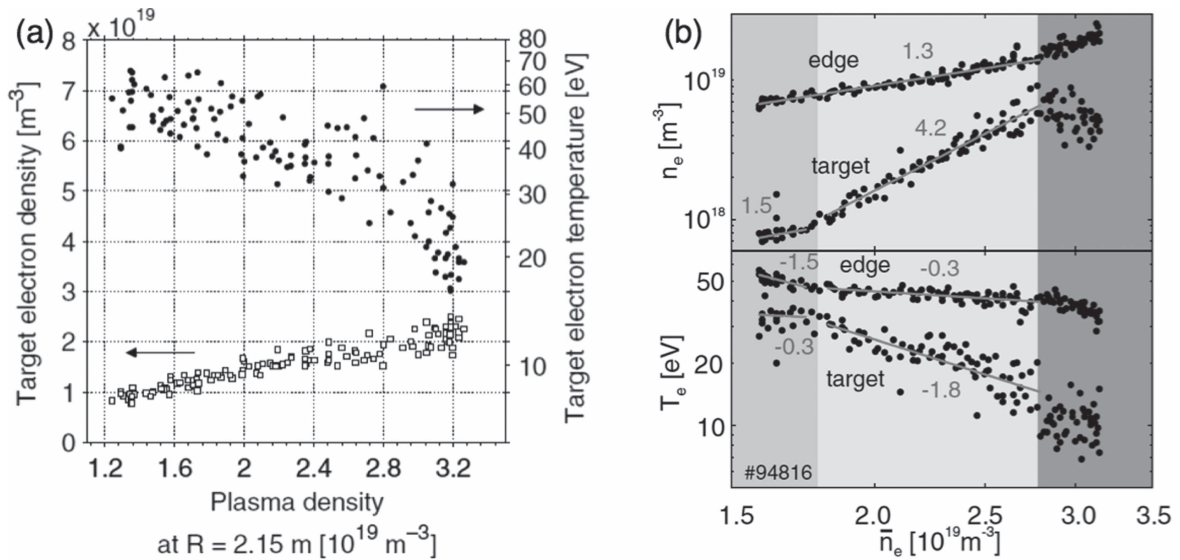
Figure 17. Target electron density and temperature measured by Langmuir probes in TEXTOR Dynamic Ergodic Divertor (DED) experiments. (a) is an example of no high recycling regime ($n_{e,target} \propto n_{e,up}^{-1}$ and $T_{e,target} \propto n_{e,up}^{-1}$) in the $m/n = 6/2$ configuration, and (b) shows that the high recycling regime has been recovered ($n_{e,target} \propto n_{e,up}^{4.2}$ and $T_{e,target} \propto n_{e,up}^{-1.8}$) even in the 3D configuration ($m/n = 3/1$). The numbers in plot (b) are the exponent of $\bar{n}_e$ for the n_e and T_e measured in the edge and target. Plot (a) is reproduced courtesy of IAEA. Figure from [59]. Plot (b) is reprinted from [60]. Copyright 2005, with permission from Elsevier.
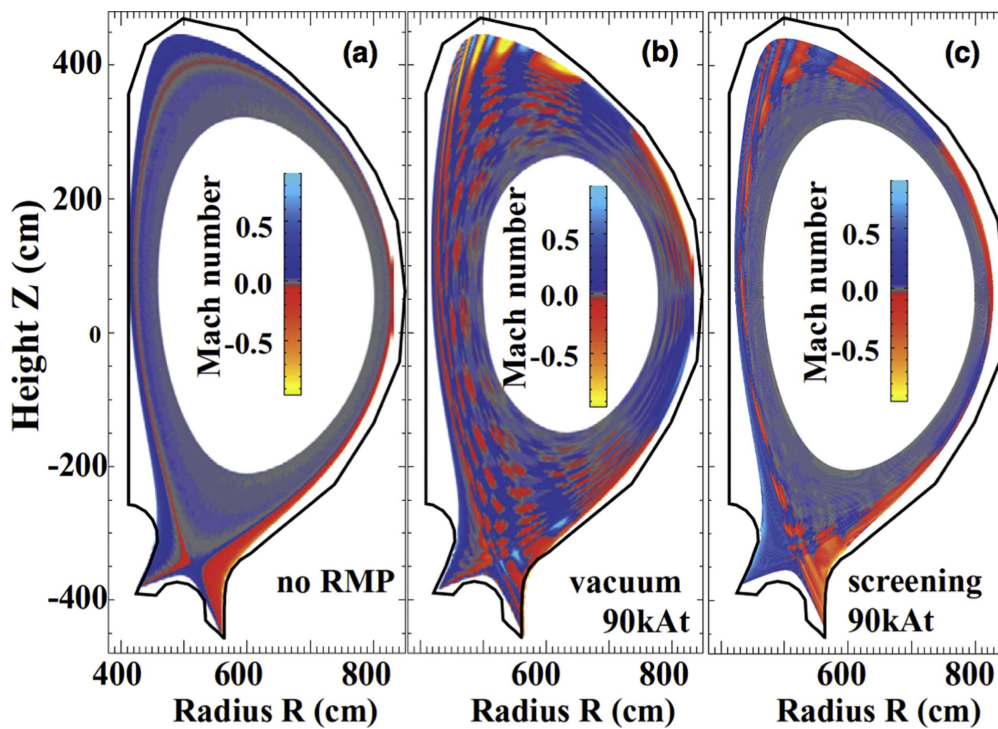

Figure 18. Poloidal cross section of parallel plasma flow for ITER without (a) and with ((b) and (c)) RMP, modeled by EMC3-EIRENE. The case of 90 kAt of the RMP coil current is shown here. Plot (b) is for the vacuum RMP case and (c) for the screened RMP. Reproduced courtesy of IAEA. Figure from [66]. Copyright (2016) IAEA.

5. Summary and discussion

Experimental and theoretical modeling results for the effect of 3D fields on divertor detachment in tokamak and stellarator have been reviewed in this paper. Experimental data for X-point divertor plasmas in NSTX ($n = 3$ mid-plane coils) and DIII-D ($n = 3$ even and odd parities) show that

detachment onset or sustainment can be interrupted by the applied 3D fields under certain conditions. 3D fields induced heat flux to burn through and re-attach a partially detached, i.e. only near the strike point, plasma in NSTX. An increase of $T_{e,ped}$ is observed along with the re-attachment. More gas puff to move the plasma into the deeper detachment allowed it to remain detached but pronounced heat flux through the

lobes in the far SOL was not suppressed. Even stronger gas puff finally removed the heat flux for the outer lobes, but resulted in significant stored energy drop ($\sim$25%). Although the plasma re-attachment is not yet reproduced in the simulation, an EMC3-EIRENE 3D edge transport modeling showed that far SOL plasma remained attached with pronounced lobe heat flux when the density was raised. The EMC3-EIRENE simulation also showed that there was no roll-over of the ion particle flux with the density increase in the range simulated in the case of $n = 3$ application.

One series of DIII-D data shows a similar trend as in NSTX; the even parity $n = 3$ fields raise the core T_e compared to the no RMP case, while the n_e is unchanged. The T_e increase is correlated with the suppression of an $n = 2$ MHD mode by the RMP and the detachment does not onset even at the density higher than the value that led to detachment in the no RMP case. This was demonstrated by the measured heat flux profiles as well as the radiated power (P_{rad}) near the X-point measured by the imaging bolometer; lower P_{rad} and higher q_{peak} in the presence of 3D fields compared to the no 3D field case. The ion saturation current profile from the target LPs and the 2D DTS data also confirmed that the OSP is attached in the 3D field case while it remained detached in the no 3D field case. However, another series of DIII-D discharges demonstrates that the detachment onset at the same Greenwald fraction ($\sim$0.7) whether the RMP was applied or not. Contrary to the case showing no detachment onset (increased core T_e) with the 3D fields, there is no change in the T_e profile by either the even or odd parity RMP. For these discharges, the detachment onset threshold remains unchanged and the heat flux profile is very similar after the detachment between the no-RMP and the RMP cases.

The density dependence of the heat flux profile behavior in DIII-D is consistent with the EMC3-EIRENE simulation result; the q_{peak} decreases and the lobe heat flux becomes less prominent as the density increases. Unlike the NSTX simulation result, the whole heat flux profile is reduced as the density is raised without pronounced heat flux in the outer lobes. The A_{wet} increases by up to $\sim$30% by the applied 3D fields in the lower density range ($0.4 < n_e/n_{GW} < 0.6$), but this difference becomes smaller as the density increases and then finally disappears when the plasma is detached in the highest density ($n_e/n_{GW} > 0.7$).

LHD demonstrated that applied RMP can stabilize detached operation, without which thermal instability leads to radiative collapse of plasma. In the presence of RMP, there is a clear T_e flattening corresponding to $n/m = 1/1$ island where the calculated radiated power increases noticeably compared to no RMP case. An EMC3-EIRENE simulation shows that RMP modifies spatial distribution of radiation belt (originally concentrated on the inboard side) and retains it around the X-point of $n/m = 1/1$ island to keep it from penetrating into the core region. The plasma response is found to play a crucial role in the transition to stable detached operation. When the phase of response fields approaches that of RMP fields so the screening currents decrease, the growth of island takes place and this enables detachment transition.

The effect of 3D magnetic geometry on divertor transport and operation can become prominent in two circumstances although they can overlap in certain conditions. The first situation is when perpendicular transport contributes substantially to the overall transport processes, such as in the stochastic layer in stellarators or in the island divertor configuration. The second is when neighboring channels of opposite flows are physically close enough to each other to lead to momentum loss via friction force. Both cases can facilitate detachment with the absence of high recycling regime before the detachment onset. However, recovery of high recycling regime by changing the ratio of perpendicular to parallel transport was observed experimentally in limiter tokamaks with 3D fields (TEXTOR and Tore Supra). This can be true even in the stellarator configuration. For example, a numerical simulation in W7-X [57] showed that the divertor plasma behavior becomes closer to that of the 2D tokamak high recycling regime, with the increase of control coil current (I_{CC}) that can be used to fine tune the internal pitch of field lines and therefore to control the perpendicular to parallel transport ratio in the islands. On the other hand, LHD needed RMP fields in addition to its intrinsic 3D configuration for a sufficient growth of island, without which stable detachment transition was more difficult. These results imply that either the increased momentum loss by the counter-flow or the enhanced perpendicular transport could assist divertor plasma to enter detachment more easily for both tokamak and stellarator.

For the X-point divertor tokamaks with 3D fields, parallel transport is still dominant in usual operating conditions and this could be the reason why 3D fields have no effect on the facilitation of detachment as seen in NSTX and DIII-D, unless there is sufficient counter-flow momentum loss between adjacent lobes. Rather, hot and dense plasma particles flowing directly from the pedestal region appear to increase $q_{\|e}$ so to raise detachment threshold density or even to re-attach detached plasma. However, the plasma response might be able to provide a way to enhance 3D effects. Both NSTX and DIII-D had limited means to control plasma response for the discharges included in this review. NSTX is unable to actively change pitch alignment because there is only one row of coils at the mid-plane. DIII-D $n = 3$ fields can only have two phases (even and odd) and 3D detachment experiments were primarily done in the even parity configuration. In the end, the plasma response screened the applied 3D fields in both NSTX and DIII-D. The screened RMP case is expected to have weaker 3D effects as shown in the EMC3-EIRENE simulation for ITER. Therefore, in a configuration where pitch alignment can be actively varied, for example $n = 2$ in DIII-D, optimal plasma response window for best 3D effects might be able to be identified.

The two key physical processes to achieve the change in the divertor regime leading to the early detachment onset, high perpendicular to parallel transport ratio ($q_{\perp e}/q_{\|e}$) and the strong counter-flow momentum loss ($f_m = \tau_{m\|}/\tau_{m\perp}$), where $\tau_{m\|}$ and $\tau_{m\perp}$ is parallel and perpendicular momentum transport time, have not yet been investigated in detail particularly

for the X-point divertor tokamaks. Tuning the $q_{\perp e}/q_{\parallel e}$ ratio is easier in 3D limiter tokamaks and stellarators by adjusting the RMP coil current, which provides more flexibility for the divertor control and optimization. However, because the parallel transport is still the dominant transport process (more true as the input power increases) in the 3D divertor tokamak configuration, i.e. $q_{\perp e}/q_{\parallel e} \ll 1$, the focus is how to achieve high f_m in the SOL of 3D tokamaks. Since the flow pattern is strongly affected by the screening or amplification of the applied 3D fields, a wide scan of parameters closely related to the plasma response, such as toroidal mode number, q_{95}, plasma triangularity (δ), normalized beta (β_N), and the relative phase difference between different row of 3D coils ($\Delta\phi_{UL}$), should be explored in order to find optimal window of parameters. Further, this window should be compatible with the window for the ELM control to be able to address both the transient and steady state heat flux issues.

The divertor conditions and footprint profiles in the desired parameter windows should be also compared to the 3D edge transport simulation results. Presently the EMC3-EIRENE code is not capable of dealing with the high radiation regime, but work is in progress to get stable solutions with the volume recombination process included [65, 66]. Both ideal and resistive plasma response models should be tested for the magnetic field model needed for the EMC3-EIRENE simulation. Modeling for various 3D configurations will enable to identify common and different physics elements toward better understanding of 3D effects on divertor conditions and detachment.

Acknowledgments

ORCID

A R Briesemester ⬤ https://orcid.org/0000-0003-3703-0978

References

[1] Evans T E *et al* 2005 *Nucl. Fusion* **45** 595
[2] Evans T E *et al* 2006 *Nat. Phys.* **2** 419
[3] Liang Y *et al* 2007 *Phys. Rev. Lett.* **98** 265004
[4] Suttrop W *et al* 2011 *Phys. Rev. Lett.* **106** 225004
[5] Jeon Y M *et al* 2012 *Phys. Rev. Lett.* **109** 035004
[6] Canik J M *et al* 2010 *Phys. Rev. Lett.* **104** 045001
[7] Canik J M *et al* 2010 *Nucl. Fusion* **50** 034012
[8] Zhu W *et al* 2006 *Phys. Rev. Lett.* **96** 225002
[9] Solomon W M *et al* 2010 *Phys. Plasmas* **17** 056108
[10] Garofalo A M *et al* 2015 *Phys. Plasmas* **21** 056116
[11] Garofalo A M *et al* 2011 *Nucl. Fusion* **51** 083018
[12] Ahn J-W *et al* 2010 *Nucl. Fusion* **50** 045010
[13] Ahn J-W *et al* 2011 *Phys. Plasmas* **18** 056108
[14] Ahn J-W *et al* 2014 *Plasma Phys. Control. Fusion* **56** 015005
[15] Ahn J-W *et al* 2014 *Proc. 25th IAEA Fusion Energy Conf. (St. Petersberg, Russia)* paper EX/P6-53
[16] Briesemeister A R *et al* 2015 *J. Nucl. Mater.* **463** 524
[17] Briesemeister A R *et al* 2016 *Proc. 22nd International Conf. on Plasma Surface Interactions in Control. Fusion Devices (Rome, Italy)* I–18
[18] Briesemeister A R *et al* 2016 *Preprint: 2016 IAEA Fusion Energy Conf. (Kyoto, Japan)* EX/7-3Rb
[19] Briesemeister A R *et al* 2017 *Nucl. Fusion* **57** 076038
[20] Petrie T W *et al* 2011 *J. Nucl. Mater.* **415** S906
[21] Petrie T W *et al* 2011 *Nucl. Fusion* **51** 073003
[22] Lore J D *et al* 2012 *Nucl. Fusion* **52** 054012
[23] Lore J D *et al* 2016 *Proc. 2016 Sherwood Fusion Theory Conf. (Madison, USA)*
[24] Lore J D *et al* 2016 *Preprint: 2016 IAEA Fusion Energy Conf. (Kyoto, Japan)* TH/P6-12
[25] Kobayashi M *et al* 2013 *Nucl. Fusion* **53** 093032
[26] Pandya S N *et al* 2016 *Nucl. Fusion* **56** 046002
[27] Kobayashi M *et al* 2010 *Phys. Plasmas* **17** 056111
[28] Kobayashi M *et al* 2015 *Nucl. Fusion* **55** 104021
[29] Grigull P *et al* 2003 *J. Nucl. Mater.* **313–316** 1287
[30] Feng Y *et al* 2005 *Nucl. Fusion* **45** 89
[31] Buttery R J *et al* 1996 *Nucl. Fusion* **36** 1369
[32] Evans T E *et al* 2005 *J. Phys.: Conf. Ser.* **7** 174
[33] Park J K *et al* 2007 *Phys. Plasmas* **14** 052110
[34] Ferraro N M *et al* 2010 *Phys. Plasmas* **17** 102508
[35] Kim K *et al* 2015 *Plasma Phys. Control. Fusion* **57** 104002
[36] Evans T E *et al* 2007 *J. Nucl. Mater.* **363–365** 570
[37] Narushima Y *et al* 2013 *Plasma Fus. Res.* **8** 1402058
[38] Narushima Y *et al* 2014 *Plasma Fus. Res.* **9** 1202066
[39] Soukhanovskii V A *et al* 2011 *Nucl. Fusion* **51** 012001
[40] Soukhanovskii V A *et al* 2012 *Phys. Plasmas* **19** 082504
[41] Mordijck S *et al* 2010 *Nucl. Fusion* **50** 034006
[42] Alfier A *et al* 2008 *Nucl. Fusion* **48** 115006
[43] Ahn J-W *et al* 2010 *Rev. Sci. Instrum.* **81** 023501
[44] McLean A G *et al* 2012 *Rev. Sci. Instrum.* **83** 053706
[45] Scotti F *et al* 2012 *Rev. Sci. Instrum.* **83** 10E532
[46] Soukhanovskii V A *et al* 2010 *Rev. Sci. Instrum.* **81** 10D723
[47] Feng Y *et al* 1997 *J. Nucl. Mater.* **241–243** 930
[48] Feng Y *et al* 1999 *J. Nucl. Mater.* **266–269** 812
[49] Frerichs H *et al* 2010 *Nucl. Fusion* **50** 034004
[50] Frerichs H *et al* 2012 *Phys. Plasmas* **19** 052507
[51] Frerichs H *et al* 2012 *Nucl. Fusion* **52** 023001
[52] Ohyabu N *et al* 1994 *Nucl. Fusion* **34** 387
[53] Kobayashi M 2017 private communications
[54] Shimomura Y *et al* 1983 *Nucl. Fusion* **23** 869
[55] LaBombard B *et al* 1995 *Phys. Plasmas* **2** 2242
[56] Feng *et al* 2002 *Plasma Phys. Control. Fusion* **44** 611
[57] Feng *et al* 2011 *Plasma Phys. Control. Fusion* **53** 024009
[58] Masuzaki S *et al* 2003 *J. Nucl. Mater.* **313–316** 852
[59] Clever M *et al* 2012 *Nucl. Fusion* **52** 054005
[60] Lehnen M *et al* 2005 *J. Nucl. Mater.* **337–339** 171
[61] Meslin B *et al* 1999 *J. Nucl. Mater.* **266–269** 318
[62] Evans T E *et al* 2014 *Proc. 25th IAEA Fusion Energy Conf. (Saint Petersburg, Russia)* EX/1–3
[63] Shafer M W *et al* 2016 *Preprint: 2016 IAEA Fusion Energy Conf. (Kyoto, Japan)* EX/P3-18
[64] Frerichs H *et al* 2015 *Phys. Plasmas* **22** 072508
[65] Schmitz O *et al* 2013 *J. Nucl. Mater.* **438** S194
[66] Schmitz O *et al* 2016 *Nucl. Fusion* **56** 066008